Article
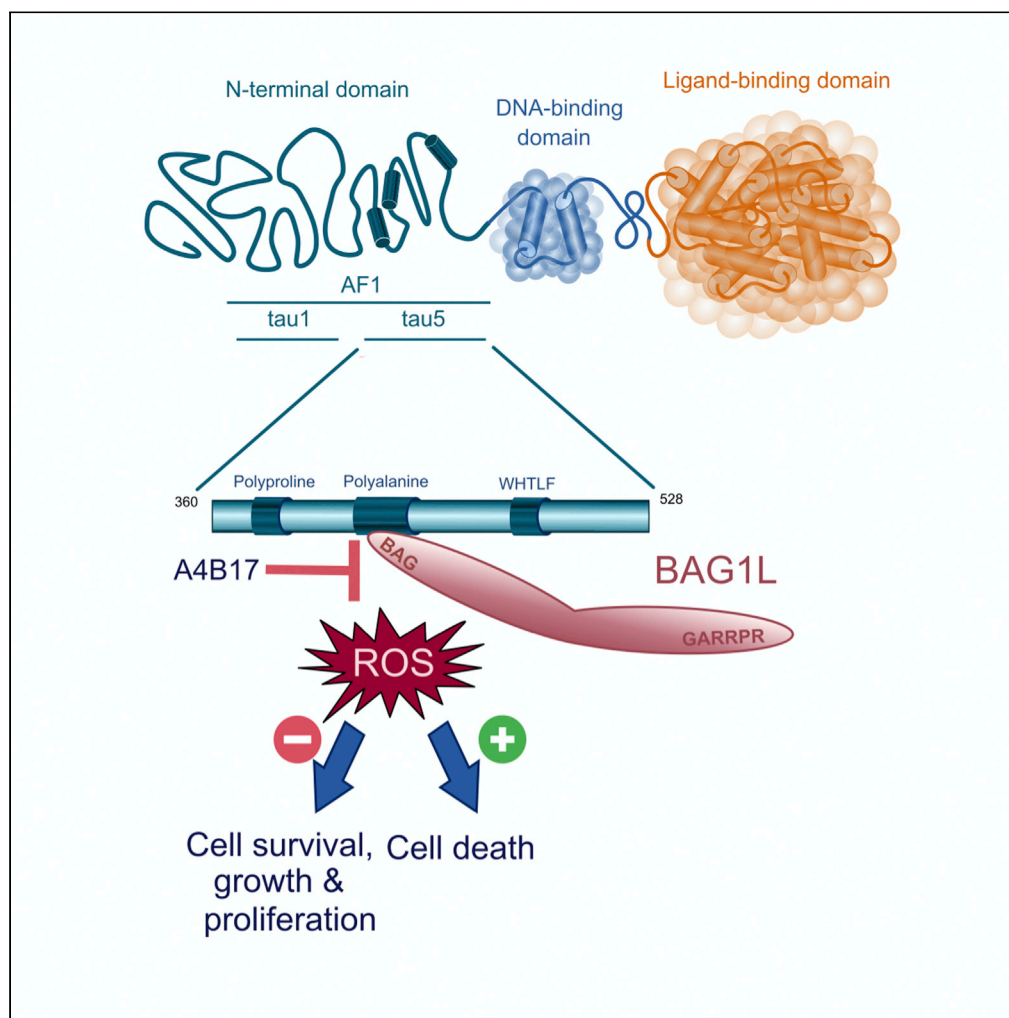
A chemical probe for BAG1 targets androgen receptor-positive prostate cancer through oxidative stress signaling pathway

Nane C. Kuznik, Valeria Solozobova, Irene I. Lee, ..., Myles Brown, Stefan Bräse, Andrew C.B. Cato

stefan.braese@kit.edu (S.B.)
andrew.cato@kit.edu (A.C.B.C.)

Highlights

BAG1L interacts with a sequence overlapping a polyalanine tract in the AR NTD

Knockdown of BAG1L increase AR dynamics in the nucleus

BAG1L uses ROS pathway to regulate AR^+ prostate cancer cell proliferation

A small molecule BAG1 inhibitor inhibits prostate tumor growth in mouse xenografts

Article

A chemical probe for BAG1 targets androgen receptor-positive prostate cancer through oxidative stress signaling pathway

Nane C. Kuznik,[1,12] Valeria Solozobova,[1,12] Irene I. Lee,[2,3] Nicole Jung,[4] Linxiao Yang,[5] Karin Nienhaus,[5] Emmanuel A. Ntim,[1] Jaice T. Rottenberg,[2,3] Claudia Muhle-Goll,[6,7] Amrish Rajendra Kumar,[1] Ravindra Peravali,[1] Simone Gräßle,[4] Victor Gourain,[8] Célia Deville,[9] Laura Cato,[2,3] Antje Neeb,[1] Marco Dilger,[1] Christina A. Cramer von Clausbruch,[1] Carsten Weiss,[1] Bruno Kieffer,[9] G. Ulrich Nienhaus,[1,5,10,11] Myles Brown,[2,3] Stefan Bräse,[4,7,*] and Andrew C.B. Cato[1,13,*]

SUMMARY

BAG1 is a family of polypeptides with a conserved C-terminal BAG domain that functions as a nucleotide exchange factor for the molecular chaperone HSP70. BAG1 proteins also control several signaling processes including proteostasis, apoptosis, and transcription. The largest isoform, BAG1L, controls the activity of the androgen receptor (AR) and is upregulated in prostate cancer. Here, we show that BAG1L regulates AR dynamics in the nucleus and its ablation attenuates AR target gene expression especially those involved in oxidative stress and metabolism. We show that a small molecule, A4B17, that targets the BAG domain downregulates AR target genes similar to a complete BAG1L knockout and upregulates the expression of oxidative stress-induced genes involved in cell death. Furthermore, A4B17 outperformed the clinically approved antagonist enzalutamide in inhibiting cell proliferation and prostate tumor development in a mouse xenograft model. BAG1 inhibitors therefore offer unique opportunities for antagonizing AR action and prostate cancer growth.

INTRODUCTION

Molecular chaperones of the HSP70 family control several cellular processes such as protein folding, protein translocation, and protein degradation. To achieve these functions, HSP70 works together with a large number of cochaperones, one of which is the nucleotide exchange factor BAG1 (Bracher and Verghese, 2015). Human BAG1 is made of a family of four polypeptides (BAG1L, BAG1M, BAG1, and BAG1S) translated from a single mRNA through different post-transcriptional mechanisms (Takayama et al., 1998; Yang et al., 1998). These include the control of 5′cap-dependent and independent translation by RNA G-quadruplex, and the use of a leaky scanning mechanism from a non-canonical CUG start codon or an internal ribosomal entry site (Coldwell et al., 2001; Jodoin et al., 2019). Structurally, the BAG1 proteins possess a conserved C-terminal BAG domain with which they bind to and regulate HSP70 activity (Sondermann et al., 2001) but divergent N-terminal regions suggesting their involvement in other isoform-specific functions in addition to their intrinsic chaperone activity (Sharp et al., 2004).

BAG1L, the largest of the BAG1 family of proteins, is the only member that is localized to the nucleus whereas the other smaller members are cytoplasmic. In the nucleus, BAG1L interacts with transcription factors such as the androgen and estrogen receptors (AR and ER) or cJun, to enhance their activity (Da Costa et al., 2010; Cutress et al., 2003; Shatkina et al., 2003). We have previously reported that BAG1L uses its conserved BAG domain to interact with the AR N-terminal domain (NTD) to enhance its activity (Cato et al., 2017; Shatkina et al., 2003). Because the AR NTD is an important domain for the transactivation function of the AR (Yu et al. 2020) and the AR a key driver of prostate cancer, small molecules targeting the BAG-AR NTD interaction interface would inhibit AR activity and function as prostate cancer therapeutics (Lee et al., 2019).

So far all currently approved prostate cancer therapies aimed at inhibiting AR action target the AR C-terminal ligand-binding domain (LBD) (Fujii and Kagechika, 2019). Although this approach is initially

[1]Institute of Biological and Chemical Systems, Biological Information Processing, Karlsruhe Institute of Technology, 76344 Eggenstein-Leopoldshafen, Germany

[2]Department of Medical Oncology, Dana-Farber Cancer Institute, Harvard Medical School, Boston, MA 02215, USA

[3]Center for Functional Cancer Epigenetics, Dana-Farber Cancer Institute, Boston, MA 02215, USA

[4]Institute of Biological and Chemical Systems, Functional Molecular Systems, Karlsruhe Institute of Technology, 76344 Eggenstein-Leopoldshafen, Germany

[5]Institute of Applied Physics, Karlsruhe Institute of Technology, 76131 Karlsruhe, Germany

[6]Institute of Biological Interfaces 4, Karlsruhe Institute of Technology, 76344 Eggenstein-Leopoldshafen, Germany

[7]Institute of Organic Chemistry, Karlsruhe Institute of Technology, 76131 Karlsruhe, Germany

[8]LabEx IGO "Immunotherapy, Graft, Oncology", Centre de Recherche en Transplantation et Immunologie - UMR1064, 44093 Nantes, France

[9]Department of Integrative Structural Biology, Institut de Génétique et de Biologie Moléculaire et Cellulaire, INSERM, U964, CNRS, UMR-7104, Université de

Continued
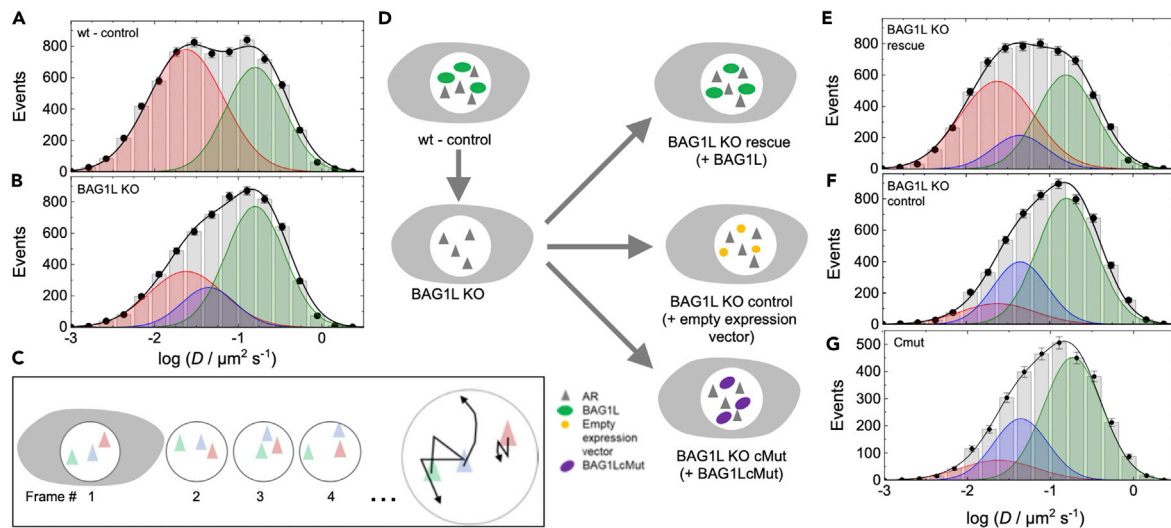
Figure 1. Loss of BAG1L alters AR dynamics in the nucleus

Histograms of the number of mEos2-AR fusion protein trajectories versus the diffusion coefficient, D (on a logarithmic scale). The data were obtained by SMT analysis of widefield fluorescence images of nuclei of (A) control and (B) BAG1L KO cells.

(C) Schematic depiction of SMT. Individual AR molecules in the cell nucleus (green, red, blue triangles) are localized by the emission from an attached fluorophore (here, mEos2) in successive image frames. The positions of each AR molecule are connected to visualize its diffusion (right, black arrows). These traces are analyzed to determine the average diffusion coefficient, (D) and standard deviations.

(D) Cells lines used in this work.

(E–G) Data obtained by SMT analysis of widefield fluorescence images of nuclei of BAG1L KO rescue, BAG1L KO control, and BAG1L KO cells transduced with mutated BAG1L.

successful, these therapies fail after about 2–3 years and patients develop a more aggressive form of the disease termed castration-resistant prostate cancer (CRPC) that, in most cases, is still dependent on AR signaling for growth (Culig et al., 2002; Galletti et al., 2017; Zegarra-Moro et al., 2002). Progression to CRPC with ongoing AR signaling is because of several factors, one of which is the expression of constitutively active AR splice variants (AR-Vs) that lack the C-terminal AR LBD but carry the N-terminal and DNA binding domains (Ware et al., 2014).

Developing inhibitors to the AR NTD is technically challenging because it is intrinsically disordered and lacks rigid pockets for drugs to bind. Several attempts to directly target this AR domain have met major setbacks (Schweizer et al., 2018). We have recently reported the development of a compound, A4B17, that disrupts the BAG1L–AR NTD interaction and inhibits the proliferation of AR positive prostate cancer cells (Kuznik et al., 2021). In this report, we present data to support a dual function of A4B17 in inhibiting AR activity. We show that A4B17 attenuates the expression of AR target genes especially those that regulate oxidative stress and metabolism in a similar manner as a BAG1L knockout. Moreover, A4B17 functions more efficaciously than the clinically approved AR antagonist enzalutamide in enhancing the expression of a subset of genes distinct from androgen responsive-genes, a number of which are oxidative stress-induced genes involved in cell death. Furthermore, A4B17 outperforms enzalutamide in a mouse xenograft model of prostate cancer under castration conditions. Collectively, these studies demonstrate that A4B17 uses both positive and negative regulatory activities to inhibit prostate cancer cell growth and identify BAG1 chemical probes as important tools for prostate cancer therapy.

RESULTS

Loss of BAG1L alters AR dynamics

BAG1L-mediated enhancement of AR activity is reported to occur through regulated AR chromatin binding (Cato et al., 2017) but it is unclear how this is triggered by the cochaperone. We therefore analyzed the impact of BAG1L on AR dynamics by single-molecule tracking (SMT) within the nuclei of BAG1L knockout (KO) and control LNCaP cells (Cato et al., 2017) using a widefield microscope with single-molecule sensitivity (Figures 1A–1C).

Strasbourg, 67404 Illkirch-Graffenstaden, France

[10]Institute of Nanotechnology, Karlsruhe Institute of Technology, 76344 Eggenstein-Leopoldshafen, Germany

[11]Department of Physics, University of Illinois at Urbana-Champaign, Urbana, IL 61801, USA

[12]These authors contributed equally

[13]Lead contact

*Correspondence: stefan.braese@kit.edu (S.B.), andrew.cato@kit.edu (A.C.B.C.)

https://doi.org/10.1016/j.isci. 2022.104175

Table 1. Single molecule tracking of mEos2AR in LNCaP cells with different BAG1L expression levels

Celltype	# Trajectories	Fraction (S1)	Fraction (S2)	Fraction (F)
Control	6881	0.60 ± 0.02	0.00	0.40 ± 0.01
Bag1L KO	8014	0.31 ± 0.01	0.16 ± 0.01	0.53 ± 0.01
Bag1L KO - rescue	6223	0.47 ± 0.01	0.13 ± 0.01	0.40 ± 0.01
Bag1L KO - control	5648	0.13 ± 0.05	0.27 ± 0.05	0.60 ± 0.05
Bag1L KO - cMut	3185	0.13 ± 0.02	0.28 ± 0.03	0.59 ± 0.02
$\log (D/\mu m^2 s^{-1})$		-1.627 ± 0.142	-1.358 ± 0.059	-0.731 ± 0.041
Diffusion coefficient, D ($\mu m^2 s^{-1}$)		0.024 ± 0.002	0.044 ± 0.002	0.186 ± 0.010
$\log (FWHM/\mu m^2 s^{-1})$		1.06 ± 0.07	0.77 ± 0.07	0.83 ± 0.07

For the SMT experiments, an N-terminal fusion construct of the AR and mEos2, a green-to-red photoconvertible fluorescent protein (Nienhaus et al., 2006) was transiently transfected into LNCaP control and BAG1L KO cells. To confirm that the results obtained are because of a loss of BAG1L, mEos2-AR was further transfected into BAG1L KO cells rescued with a BAG1L wild-type (BAG1L rescue), or transfected with an empty expression vector (BAG1L KO control) or overexpressing a mutant BAG1L defective in AR binding (BAG1LcMut) (Cato et al., 2017) (Figures 1A, 1B, and 1D–1G). We note that the BAG1L KO control, BAG1L rescue, and BAG1LcMut cells were obtained from the BAG1L KO cells by a different selection protocol than the one used in generating the BAG1L KO cell line from the wild-type control cells (Cato et al., 2017). Therefore, although the rescue cells could be compared with each other, they should not be directly compared with the control and BAG1L KO cell lines.

Before the SMT experiments, the cells were treated with 10 nM dihydrotestosterone (DHT) for 2 h. Image sequences were taken with 30 ms camera dwell time for a total of 2 min per cell. The use of weak 405-nm irradiation to sparsely photoconvert mEos2 to its red-emitting form and 561-nm light for fluorescence excitation of this species allowed us to record trajectories of individual mEos2-AR molecules (Figure 1C). These were extracted from the image sequences and analyzed to yield diffusion coefficients, D. The data are shown in Figures 1A and 1B, and 1E- 1G as histograms of the number of events (trajectories) versus the (decadic) logarithm of D. For all five cell lines, the histograms can be well fitted with a sum of three Gaussian distributions, representing fractions with distinctly different dynamics. Global fits were performed, declaring the widths and center positions (average D values) as shared parameters with the assumption that the same three AR populations are present in all cell types but at different ratios. These values are compiled in Table 1, together with the fractional populations returned by the fits and the number of trajectories. We note that the significant widths of the distributions originate predominantly from the fact that single mEos2-AR molecules can only be tracked for a few frames, which results in a large uncertainty in the determination of D from an individual trajectory. However, taking an average over a large ensemble of trajectories allowed us to determine D with high precision.

A fast-diffusing fraction, AR_F (shaded green), with diffusion coefficient, $D_F = 0.186 \pm 0.010 \mu m^2 s^{-1}$ was identified in all the samples (Table 1). This fraction is not diffusing freely but possibly experiencing brief and non-specific binding events because of random collisions and it increased from 0.40 ± 0.01 in the control cells to 0.53 ± 0.01 in the BAG1L KO cells (Table 1). A comparable increase was found when the BAG1L-rescue cells were compared with their corresponding vector transduced cells or BAG1LcMut cells (Table 1), indicating that the lack of BAG1L or BAG1L with an impaired binding to the AR favors faster diffusion of the AR.

Two Gaussians were identified associated with slowly diffusing fractions, AR_{S1} (shaded red) and AR_{S2} (shaded blue), centered on $D_{S1} = 0.024 \pm 0.002 \mu m^2 s^{-1}$ and $D_{S2} = 0.044 \pm 0.002 \mu m^2 s^{-1}$. These values are in the same range as the ones reported for AR-YFP and histone H2B-YFP ($D = 0.056 \pm 0.003 \mu m^2 s^{-1}$ and $0.040 \pm 0.0023 \mu m^2 s^{-1}$) (Van Royen et al., 2014) as chromatin binding factors and could represent specific and non-specific binding to chromatin. In the control cells, only a single slow fraction, AR_{S1}, was identified but in the BAG1L KO cells, this fraction was reduced by 50% to generate AR_{S2} in the ratio 0.31 (AR_{S1}) to 0.16 (AR_{S2}). Because AR chromatin binding is reduced in the BAG1L KO cells in our previous ChIP-seq studies (Cato et al., 2017), the AR_{S1} fraction most likely represents specific binding of AR to chromatin. Support for this comes from the finding that AR_{S1} is increased in the BAG1L KO-rescue cells, compared to its

iScience
Article
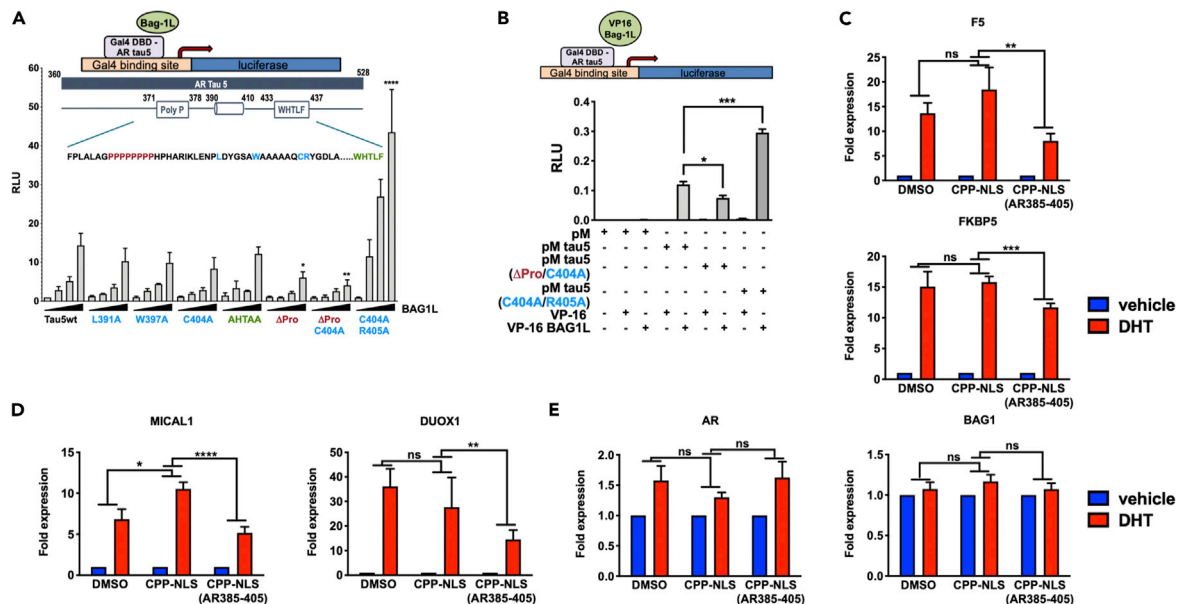
Figure 2. BAG1L binding sites and regulation of androgen-mediated ROS gene expression Identification of BAG1L regulatory element in ARτ5

(A) Mammalian one-hybrid assay in HeLa cells transfected with the indicated ARτ5 constructs linked to Gal4 DBD and increasing concentrations of BAG1L. The results are the mean of at least three independent experiments ±SEM, relative to the empty BAG1L expression vector. *p ≤ 0.05, **p ≤ 0.01 and ****p ≤ 0.0001.

(B) Mammalian two-hybrid assay performed in HeLa cells transfected with the indicated ARτ5 constructs linked to Gal4 DBD in the presence of BAG1L-VP16 fusion plasmid or VP-16 plasmid. The results show the mean of three independent experiments ±SEM *p ≤ 0.05 and ***p ≤ 0.001. RLF stands for relative luciferase activity.

(C–E) Quantitative RT-PCR showing androgen-mediated gene expression of BAG1L-target genes in LNCaP cells in the presence and absence of a control peptide (CPP-NLS) or the BAG1L binding site peptide (CPP-NLS-AR 385-405). The bar charts represent the average relative gene expression ±SEM (n = 4–7, *: p < 0.05, **: p < 0.01, ***:< p 0.001, ****: p < 0.0001). See also Figures S1–S3.

---

control (BAG1L KO control) or the BAG1LcMut cells. This is consistent with our ChIP-seq results that AR binding to chromatin is compromised in the BAG1L KO control and BAG1LcMut cells but increased in the BAG1L-rescue cells (Cato et al., 2017). Thus, BAG1L-mediated effects on AR dynamics correlate well with its effects on AR chromatin binding events.

BAG1L binding site and regulation of androgen-mediated ROS gene expression

Because AR dynamics require prior interaction of BAG1L with the AR, we sought to determine the precise interaction site of this cochaperone on the AR NTD. We have previously identified ARτ5 as a binding domain for BAG1L in the AR NTD (Cato et al., 2017; Shatkina et al., 2003), but we now use mutational studies to fine map the binding site. We carried out a mammalian-one-hybrid experiment in which the transactivation functions of a wild-type and mutant ARτ5 constructs were analyzed in the presence of increasing amounts of BAG1L (Figure 2A). Alanine substitutions of amino acid residues at L391, W397 and C404 that displayed reduced resonance intensities upon interaction with the BAG domain in our previous NMR experiments (Cato et al., 2017) did not alter the gene expression enhancing effect of BAG1L. The same observation was made for ARτ5 constructs where the activation motif WHTLF (Dehm et al., 2007) was changed to AHTAA (Figure 2A). Instead, deletion of the polyproline sequence particularly in combination with C404A (ΔPro/C404A) decreased BAG1L action whereas a double mutation C404A/R405A that extended the polyalanine residues rather enhanced BAG1L action (Figure 2A). We next demonstrated in a mammalian-two-hybrid experiment that the enhancing or inhibitory action of BAG1L toward the ARτ5 mutations occurred through changes in interaction of the two proteins. In this assay, yeast Gal4-DBD (pM) alone was not able to increase the activity of a Gal4 reporter gene, not even when it was cotransfected with the activator VP16. Neither did Gal4-ARτ5 produce any transactivation on its own. However, transactivation was observed when Gal4-ARτ5 was expressed with VP16-BAG1L indicating an interaction of ARτ5 with BAG1L. We showed that the amino acid substitutions that extended the polyalanine tract in ARτ5 increased binding to BAG1L whereas the ΔPro/C404A mutation reduced interaction (Figure 2B).

The interaction between BAG1L and ARτ5 was further investigated by mapping the interaction region of the ARτ5 fragments on the BAG1L protein surface using ^{1}H, ^{15}N NMR chemical shift perturbation experiments. Peptides covering regions of ARτ5 previously identified as potential binding sites were added to a sample of ^{15}N-labeled BAG domain and the composite chemical shift differences were reported for each residue of BAG1L sequence (Figure S1A). Peptide PM206 that covers both the polyproline and polyalanine sequences in ARτ5 caused small but distinct chemical shifts in the BAG domain sequence whereas these perturbations were not observed for peptide PM205 that covers only the polyproline and upstream sequences (Figures S1B and S1C) (see Figure S1D for the entire spectrum). Intriguingly, the perturbation pattern observed for PM206 was identical to the one generated by PM153, a smaller fragment restricted to the polyalanine sequence adjacent to PM205 (Figure S1C). Other regions of the AR NTD analyzed in this study did not produce any significant chemical shift perturbations.

Thus, the ARτ5 region encompassing the polyalanine stretch encoded in the PM153 peptide was identified as a specific low-affinity binding site for the BAG domain. Note that PM153 carries the polyalanine stretch that has previously been reported to adopt a partially folded structure in an unfolded AR NTD (McEwan, 2012; DeMol et al., 2016) and has been suggested as a potential interaction site for *trans*-acting factors. An extended alanine stretch tends to fold into α-helices and would further increase folding (Bernacki and Murphy, 2011) providing a possible explanation for the increased BAG1L effect observed for the double C404A/R405A mutant. The absence of a direct interaction between the polyproline region and BAG1L suggests an allosteric action of the proline rich region on the BAG1L/ARτ5 interaction through either conformational changes or modulation of ARτ5 self-association properties. The amino acids in the BAG domain with resonances perturbed by the interaction (E283, E326, N328, V325, and K279 in Figure S1B) map to a region that is next to the HSC70 binding site but does not form part of the BAG1/HSC70 binding interface (Briknarova et al., 2001) (Figure S1E). This suggests that the HSC70/HSP70 and AR binding sites on the BAG domain are non-overlapping and could therefore be targeted separately.

To determine whether the interaction of BAG1L with the AR NTD and its effect on AR dynamics target a distinct subset of AR-regulated genes, we reanalyzed our previous RNA-seq datasets in the control and BAG1L KO cells (Cato et al., 2017) by calculating the fold change in androgen-mediated expression of each gene using a fold difference cutoff of 1.5. The expressed genes were plotted as scatterplot matrix with LNCaP control vehicle (EtOH) versus DHT-regulated genes plotted on the x-axis and LNCaP BAG1L KO EtOH vs DHT-regulated genes plotted on the y-axis (Figure S2A). We then performed gene ontology analysis using the Broad Institute Molecular Signature Database (MSigDB) (Liberzon et al., 2011; Subramanian et al., 2005) and found, as previously reported, that most of the BAG1L-regulated genes were associated with 'androgen response'. In addition, we discovered that several of the BAG1L-regulated androgen response genes are associated with oxidative stress and metabolic processes (Figure S2B). These genes are indicated purple in Figure S2A, and some of them are labeled. Quantitative RT-PCR studies carried out to validate the expression of a select number of genes identified the classical androgen-regulated genes *KLK3*, *FKBP5* and *Proaccelerin (F5)* (Klee et al., 2012), as well as androgen-regulated redox genes *MICAL1*, *DUOX1* and *NNT* as significantly impaired by the loss of BAG1L (Figure S2C). MICAL1 is a multi-domain flavoprotein monooxygenase ROS producing enzyme involved in cancer cell growth and survival (Deng et al., 2018), and dual oxidase 1 (DUOX1) is also an ROS producing enzyme. Nicotinamide nucleotide transhydrogenase (NNT) is a mitochondrial redox-induced proton pump that links NADPH synthesis to the mitochondrial metabolic pathway. These enzymes are all involved in mitochondrial and extra-mitochondrial redox reactions either to regenerate NADPH from NADH (Li et al., 2018) or to catalyze redox reactions using NADPH as a co-enzyme (Alto and Terman, 2018).

We evaluated whether the BAG1L-mediated regulation of the AR-target genes could be linked to BAG1L interaction with the polyalanine track at the AR NTD by allowing prostate cancer cells to take up a FITC-labeled version of PM153 peptide tagged with a nuclear localization signal sequence (NLS) and a cell-penetrating peptide (CPP). As a control, we used FITC-labeled CPP-NLS peptide without the AR sequence. The rationale of the study was to determine whether the N-terminal PM153 sequence is an important contributor to AR action and whether it could squelch potential endogenous binding factors (including BAG1L) needed for AR activity. In fluorescence microscopy studies, the control and AR peptides were efficiently taken up by the cells as illustrated by the results in LNCaP cells (Figure S3A). The control CPP-NLS peptide had no effect or increased the DHT response compared to the vehicle (DMSO)-treated cells. In contrast, the peptide with the AR sequence (CPP-NLS AR 385-405) decreased androgen response as illustrated by the

downregulation of some of the AR target genes (*F5* and *FKBP5)* (Figure 2C), including the redox genes (*DUOX1, MICAL1)* that were also downregulated in the BAG1L KO cells (Figure 2D). The inhibitory effect of the peptide was not unspecific as the expression of other genes such as the *AR* or *BAG1* was not altered in the absence or presence of hormone (Figure 2E). To exclude a cell line specific effect, we also carried out peptide uptake studies in the CRPC prostate cancer cell line LNCaP95 and similar results were obtained (Figure S3B).

A4B17 attenuates the expression of androgen response genes

We next used the small molecule A4B17 that we have recently reported to disrupt the BAG1L–AR NTD interaction (Kuznik et al., 2021) to determine whether it would inhibit AR action similarly to what we reported for the BAG1L KO cells. RNA-seq experiments were first carried out in LNCaP cells treated with either vehicle, DHT, A4B17, or A4B17 + DHT and Gene Set Enrichment Analysis (GSEA) was performed to identify pathways that are enriched in each dataset. We found that the Hallmark Androgen Response pathway is enriched in the DHT dataset, but significantly attenuated in the A4B17 + DHT dataset (Figure 3A). We further found that the Hallmarks Fatty Acid Metabolism and Cholesterol Homeostasis were also significantly attenuated in the A4B17 + DHT dataset when compared to the DHT only treatment. Because lipid biosynthetic pathways are major AR targets (Han et al., 2018; Zadra et al., 2019), our finding that they are downregulated by A4B17 provides significant evidence of AR antagonistic properties of A4B17. Quantitative RT-PCR experiments confirmed A4B17-mediated downregulation of the classical AR targets (e.g *KLK3* and *FKBP5)* as well as genes in the redox and metabolic pathways (*MICAL1, SAT1, DUOX1,* and *GNMT*) (Figure 3B). We next compared our A4B17 RNA-seq dataset with the differential regulated genes derived from the BAG1L KO matrix (Figure S2A) and found in the heatmap that a number of genes, especially those involved in redox homeostasis, were regulated similarly between A4B17 and BAG1L KO datasets (Figure 3C). As further proof that A4B17 functions through BAG1L, we carried out quantitative real-time PCR studies on a select number of genes identified in the heatmap to show that the inhibitory action of A4B17 was absent or impaired in the BAG1L KO cells compared to the control cells (Figure 3D).

The link between BAG1L and the oxidative stress pathway was further established by determining the level of reactive oxygen species (ROS) produced in the control compared to the KO cells using the fluorescent probe 2',7'-dichlorofluorescein diacetate (DCF). Treatment of control LNCaP cells with the synthetic androgen R1881 resulted in a small but significant increase in ROS production as previously reported (Basu et al., 2009; Ripple et al., 1997). Strikingly, the ROS level in the BAG1L KO cells was strongly reduced and did not show any further increase upon R1881 treatment (Figure 3E). We also showed that R1881-mediated increase in ROS is reduced in LNCaP cells by A4B17 (Figure 3F).

We then used the flavoprotein inhibitor diphenyleneiodonium (DPI) that blocks ROS production resulting from the action of NAD(P)H oxidases (Altenhöfer et al., 2015; O'Donnell et al., 1994) to demonstrate the involvement of ROS in BAG1L action. Proliferation in control and BAG1L KO LNCaP cells was analyzed in the presence of DPI. Although proliferation of the control cells was decreased by DPI this did not occur in the BAG1L KO cells that already showed a reduced proliferation (Figure S4). Combined, these results show that BAG1L controls AR activity and proliferation in part, via the production of ROS.

A4B17 action in different prostate cancer cell lines

As A4B17 interacts with the conserved BAG domain of BAG1 (Kuznik et al., 2021), it may control the action not only BAG1L but also the cytoplasmic BAG1 proteins previously reported to present client proteins to the proteasome for degradation (Abildgaard et al., 2020; Demand et al., 2001; Hantouche et al., 2017). We therefore assessed whether changes in AR expression levels occur in immunoblot assays when LNCaP (control and BAG1L KO) and 22Rv.1 cells were treated with A4B17 (10^{-9}– 10^{-5} M). A slightly reduced AR level was detected at the highest A4B17 concentration (10^{-5} M) (Figure S5), suggesting that destabilization or degradation of AR may contribute to the attenuation of AR's activity. Under the same conditions, the level of the BAG1 proteins was not altered. The only difference observed in BAG1 levels was the reported increased expression of the cytoplasmic BAG1 proteins that occurred following the knockout of BAG1L (Cato et al., 2017).

We next used the control and BAG1L KO LNCaP cells in clonogenic experiments to determine whether the reported inhibition of proliferation of AR-positive cells by A4B17 (Kuznik et al., 2021) also required
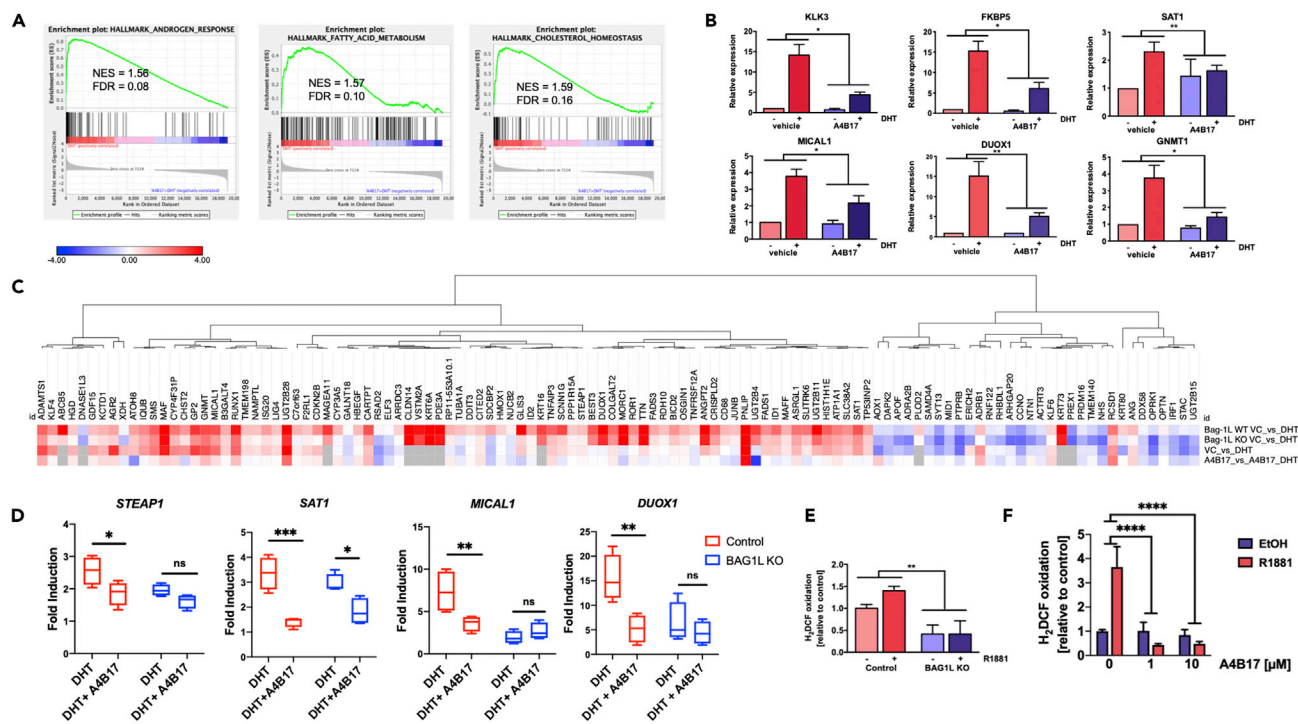
Figure 3. A4B17 attenuates the expression of androgen response genes

(A) A4B17 attenuates the expression of androgen response genes. Gene set enrichment analysis from RNA-seq data comparing DHT to A4B17 + DHT treatment showing AR response, fatty acids metabolism and cholesterol homeostasis enrichment plots.

(B) Quantitative real-time PCR analysis showing the attenuation of expression of some of the AR target genes identified in the RNA-seq studies. The bar charts represent the mean $\pm$ SEM of 6–7 independent experiments (*: p < 0.05; **: p < 0.01).

(C) Changes in AR target gene expression mediated by A4B17 treatment compared to BAG1L KO. Heatmap of differentially regulated AR target genes in control (BAG1L WT), and BAG1L KO LNCaP cells compared with changes in AR target gene expression in LNCaP cells treated with DHT, or A4B17 + DHT datasets.

(D) Quantitative real-time PCR analysis showing the effect of A4B17 on DHT-mediated expression of select genes in the redox and metabolic pathways in control and BAG1L KO LNCaP cells. The bar charts represent the mean $\pm$ SEM of 6-7 independent experiments (*: p < 0.05; **: p < 0.01, ***: p < 0.001, n.s. not significant).

(E and F) Reduced 2′7-dichlorofluorescein diacetate (H$_2$DCF) oxidation assay showing an impaired reactive oxygen species (ROS) production in control compared to BAG1L KO LNCaP cells. ROS production was determined in control and BAG1L KO LNCaP cells treated with 10^{-8} M androgen (R1881) for 96 h. The results represent the averages of H$_2$DCF oxidation $\pm$SEM (**p < 0.01 n = 6).

(F) ROS production in LNCaP cells treated with the indicated concentrations of A4B17 for 96 h and 10^{-8} M androgen (R1881) for 72 h. The results represent the averages of H$_2$DCF oxidation $\pm$SEM (****p < 0.0001 n = 1 with 6 technical replicates). Also see Figure S4.

the cytoplasmic BAG1 proteins. Clonal expansion of the control LNCaP cells was inhibited with an IC$_{50}$ of 2.81 $\pm$ 0.70 μM whereas an approximately 10-fold higher concentration (IC$_{50}$ = 20.59 $\pm$ 2.36 μM) was needed for the inhibition of the BAG1L KO cells (Figures 4A and 4B). Thus, it appears that all BAG1 proteins contribute to A4B17 action not only in the regulation of AR-target gene expression but also in the control of proliferation of AR-positive cells. Intriguingly, we noticed in the clonogenic experiments that A4B17 inhibited the clonal expansion of estrogen receptor (ER)-positive MCF-7 and ZR75-1 breast cancer cells (IC$_{50}$ = 1.28 and 0.11 μM respectively) but not ER-negative MDA-MB231 cells (Figure 4C). This finding is most likely because of the reported enhancing action of BAG1 proteins on ER activity (Cutress et al., 2003).

To determine the efficacy of A4B17 as an AR antagonist, we compared its action with that of the clinically approved AR antagonist enzalutamide on the viability of three AR positive PCa cell types (LNCaP, LAPC-4 and 22Rv.1). In LNCaP cells with a mutant AR (Veldscholte et al., 1990), A4B17 was less efficacious than enzalutamide (Figure 4D) whereas in the enzalutamide resistant CRPC cell line 22Rv.1 with AR mutations and truncations (Li et al., 2013a; Marcias et al., 2010), A4B17 decreased cell viability albeit at increased concentrations (IC$_{50}$ = 8.51 μM) (Figure 4E). In contrast, in LAPC-4 cells that express wild-type AR (Klein et al., 1997),
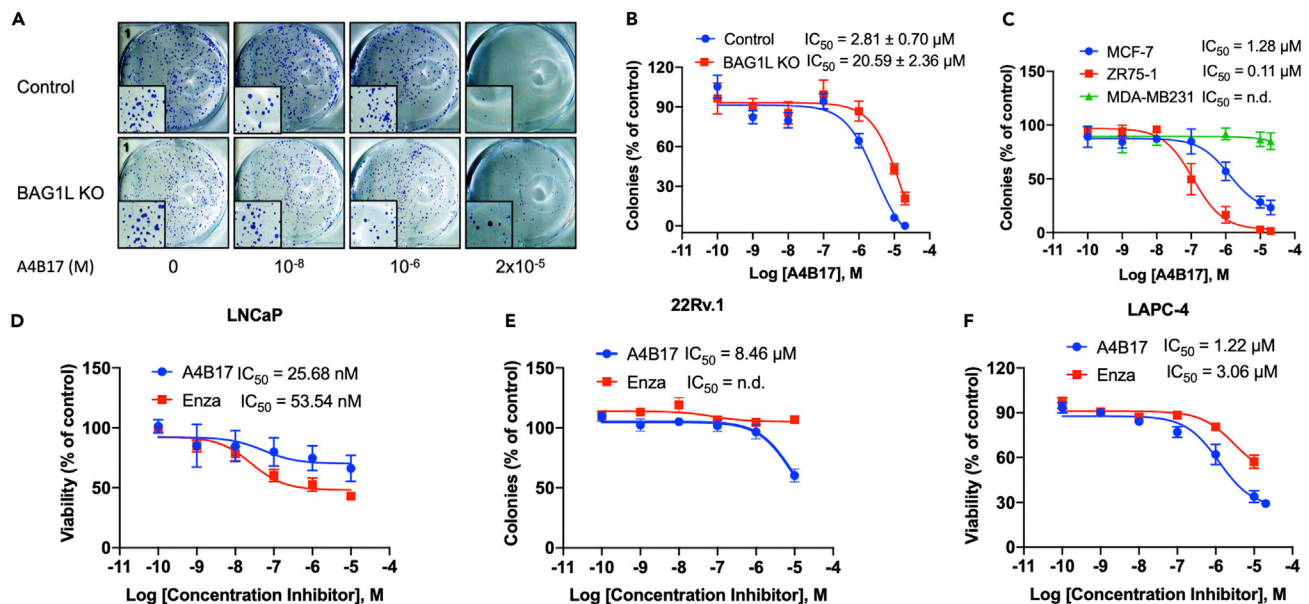
Figure 4. A4B17 action in different cancer cell lines

(A) Clonogenic cell survival assay showing representative images of the colonies formed in control and BAG1L KO LNCaP cells following treatment with the indicated concentrations of A4B17.

(B) Quantification of the colonies of three different experiments each with three biological replicates. The results are presented relative to the colonies formed in the vehicle-treated samples which was set at 100% (n = 9) and are the averages ±SEM.

(C) Quantification of the colonies formed by the different cell lines after treatment with the indicated concentrations of A4B17. The results are presented relative to the colonies formed in the vehicle-treated samples which was set at 100% (n = 3) and are the averages ±SEM.

(D–F) MTT assay to determine the effect of the indicated concentrations of enzalutamide or A4B17 on the viability of LNCaP (n = 3), 22Rv.1 cell (n = 4; n.d. not determinable) and LAPC-4 (n = 7) cells. The IC_{50} results are the averages ±SEM. Also see Figure S5.

A4B17 was slightly better than enzalutamide both in potency and efficacy in decreasing cell viability (Figure 4F). We therefore used LAPC-4 cells and performed transcriptomic experiments to identify what contributes to its improved activity over enzalutamide after treating the cells with each of the two compounds (5 μM) for 16 h.

A4B17 shows enhanced activity over enzalutamide

On the whole, very few differentially expressed genes (DE-Gs) were identified following both treatments but those detected were mostly upregulated genes (Figures 5A and 5B). This is in agreement with previous reports of enzalutamide enhancing the expression of a novel subset of genes in prostate cancer cells that are distinct from androgen-responsive genes (Yuan et al., 2019). There were 22 enzalutamide DE-Gs compared to 231 A4B17-regulated genes. However, about 63% of the enzalutamide DE-Gs were also found regulated in a similar pattern in the A4B17-treated cells (Figure 5C) suggesting a substantial degree of overlap in the action of the two compounds. Some of the published enzalutamide upregulated genes (Yuan et al., 2019) that are also transcriptionally enhanced by A4B17 inhibit cellular growth such as ferritin heavy chain 1 (*FTH1*) that catalyzes the generation of reactive oxygen species (ROS) through Fenton chemistry (Arosio and Levi, 2010), oxidative stress-induced heme oxygenase 1 (*HMOX1*) whose upregulation is associated with less aggressive prostate cancer phenotype (Gueron et al., 2009), and oxidative stress-induced growth inhibitor 1 (OSGIN1) that inhibits growth and cellular apoptosis in a variety of carcinoma cells (Hu et al., 2012a; Tsai et al., 2017) (Figure 5C). In addition, there were other genes whose expression was uniquely regulated by A4B17 but were too few for GO-term analysis. However, some of these genes are involved in the regulation of prostate cancer and together these findings underscore mechanistic differences in the action of A4B17 and enzalutamide (Table S1).

Quantitative RT-PCR validation of a select number of the DE-Gs identified in the transcriptomic analysis showed a higher upregulation of expression by A4B17 compared to enzalutamide, suggesting an overall stronger action of A4B17 on these genes (Figure 5D). This trend was also observed in the AR-positive
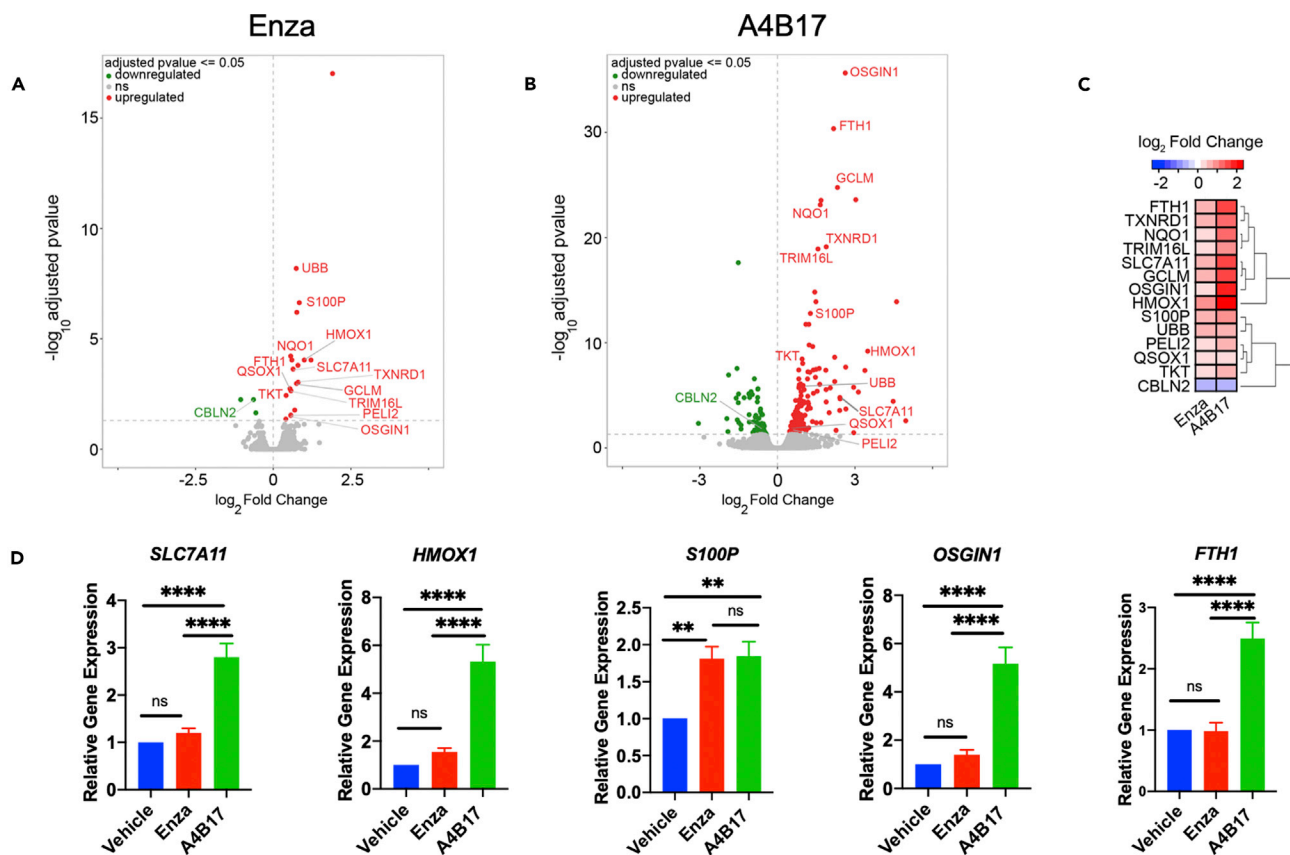
Figure 5. A4B17 shows enhanced activity over enzalutamide

Transcriptomic experiments showing changes in gene expression after treatment of LAPC-4 cell with 5 μM A4B17 and enzalutamide for 16 h. Volcano plots showing changes in expression of genes dysregulated by A4B17 and enzalutamide. Genes were considered dysregulated if associated with an adjusted p-value (y-axis) of 0.05 (horizontal dashed line). No threshold was applied on log2 (fold change). Upregulated genes are plotted in red, downregulated ones in green, and non-regulated genes in gray.

(C) Heatmap showing hierarchical clustering of 14 common genes dysregulated by both A4B17 and enzalutamide.

(D) Quantitative real-time PCR analysis showing the effect of A4B17 and enzalutamide on select genes identified in the heatmap. The results represent the mean ± SEM (n = 8, p values are **: p = 0.002, ****: p < 0.0001, n.s: not significant). Also see Figure S6 and Tables S1.

22Rv.1 CRPC cell line (Figure S6A) but not in the AR-negative PCa cell lines PC3 or DU145 (Figures S6B and S6C). It is notable that several of these genes are oxidative stress-induced genes and cells whose proliferation was inhibited by A4B17 (Kuznik et al., 2021) showed increased expression of these genes.

A4B17 outperforms enzalutamide in tumor growth inhibition

A4B17 belongs to a class of benzothiazole-based compounds with a broad spectrum of biological activities (Irfan et al., 2020) that could display off-target effects. We therefore analyzed its potential side effects in zebrafish, a well-recognized biological model for toxicology research that allows for quick and large scale screening in a whole-organism biological system with highly conserved organ systems and metabolic pathways (Horzmann and Freeman, 2018). A4B17 effects were compared with enzalutamide in overall mortality and hatching rate of zebrafish embryos (Huang et al., 2018). Cumulative mortality was high at 24, 48, 72, and 96 h post fertilization (hpf) when 30 μM but not when 10 μM A4B17 or enzalutamide was used (Figure 6A). For hatching rate determinations that begin typically between 48 and 72 hpf (Kimmel et al., 1995), no overt adverse effects were observed at 10 or 30 μM A4B17 whereas 30 μM but not 10 μM enzalutamide completely blocked the embryos from hatching at 72 and 96 hpf (Figure 6B). These findings are consistent with published toxic effects of enzalutamide observed at concentrations higher than 10 μM in the zebrafish model (Melong et al., 2017). The zebrafish results therefore identified A4B17 as non-toxic at 10 μM and slightly less toxic than enzalutamide at 30 μM.
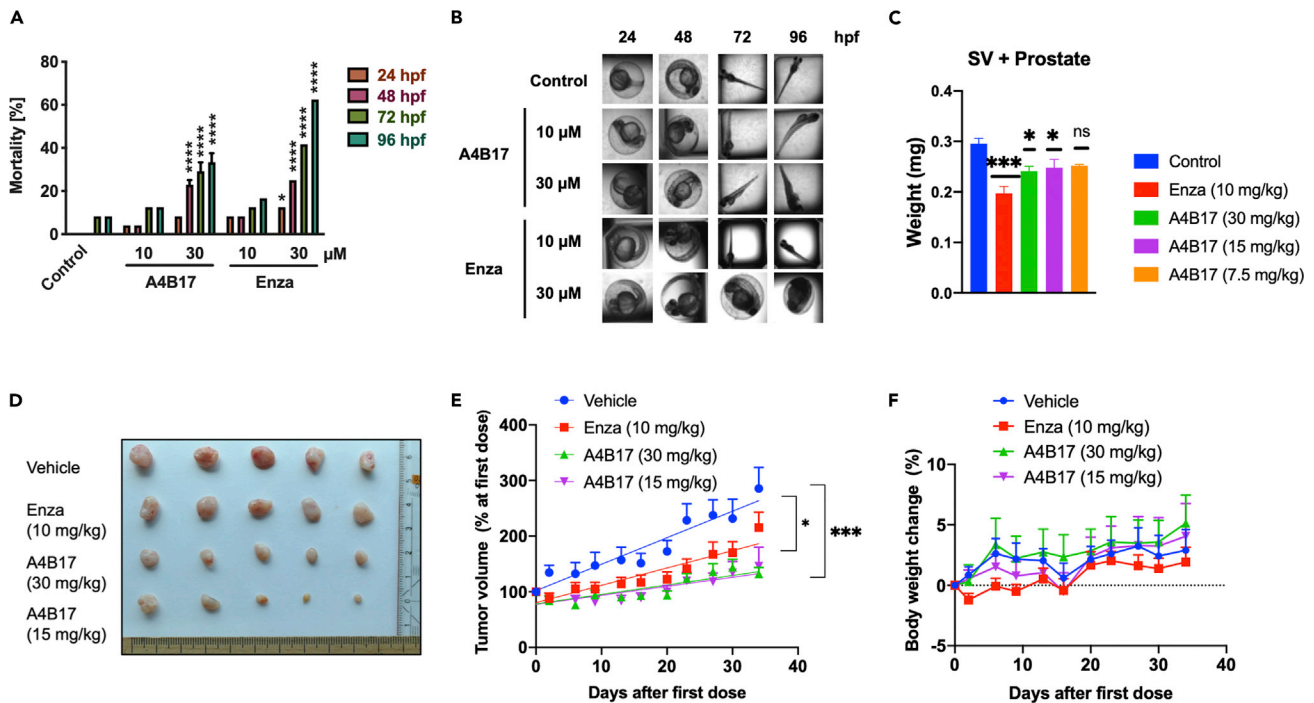
Figure 6. A4B17 outperforms enzalutamide in tumor growth inhibition

(A) Assessment of compound toxicity in developing zebrafish embryos. The bar chart represents mortality rates of 48 zebrafish embryos in percentages following exposure to the indicated compounds. The results represent the averages of two biological replicates (*: p < 0.05, and ****: p < 0.0001).

(B) Images of examples of the embryos before and after hatching (24–96 hpf) following exposure to the indicated compounds. The images were taken with an automated Scan^R IX 81 microscope (with Olympus Planapo lens 1.25x).

(C) Comparison of the effect of the indicated concentrations of A4B17 and enzalutamide (10 mg/kg) on prostate and seminal vesicle weights following a 14-day treatment. The results represent the mean ± SEM (n = 3, *p < 0.05, ***: p < 0.001).

(D) Representative examples of some of the tumors obtained after treatment with vehicle, enzalutamide and A4B17.

(E) Tumor volumes of established subcutaneous LAPC-4 xenografts obtained after castration and a 7-day recovery followed by daily treatment for 34 days with vehicle, enzalutamide (Enza, 10 mg/kg body weight), or A4B17 (15 mg/and 30 mg/kg body weight). The values are the mean ± SEM expressed relative to the initial tumor volume at the start of treatment, which was set at 100%. (n = 7 for each group, *: p = 0.0240, ***: p ≤ 0.0001).

(F) Mice body weights were measured twice weekly for all animals over the 34 days treatment period. Presented are the mouse body weight changes, in percentages, for each group. Also see Figures S7 and S8.

We also tested the action of the two compounds in mice following daily oral gavage of 7.5–30 mg/kg A4B17 or 10 mg/kg enzalutamide over two weeks. Among all the organs analyzed, a decrease in the weight of the prostate and seminal vesicles by enzalutamide (10 mg/kg) and A4B17 (15 mg/kg and 30 mg/kg) was the only significant difference detected (Figures 6C and S7), suggesting anti-androgenic actions of the two compounds at the indicated concentrations. The lack of an obvious toxic effect of A4B17 in human cells, mice and in the zebrafish model reflects selective engagement of the compound to the BAG pocket in these species. BAG1 is a very conserved protein and the BAG domain, especially the amino acids that form the BAG pocket into which A4B17 docks (Kuznik et al., 2021), is conserved in human, mice and zebrafish (Nguyen et al., 2020).

We next used the LAPC-4 prostate cancer cells with the wild-type AR in a mouse xenograft model where castration was performed to mimic an androgen deprivation phenotype before treatment of the mice with A4B17 (15 and 30 mg/kg) and enzalutamide (10 mg/kg). Because LAPC-4 cells are strictly dependent on androgens for proliferation (Garcia et al., 2014), the development of LAPC-4 tumors in the castrated mice was rather slow. Nonetheless, both enzalutamide and A4B17 further reduced tumor growth (Figures 6D and 6E) with the latter showing a better inhibition profile despite the stronger action of enzalutamide in the reduction of the weight of the prostate and seminal vesicle (Figure 6C). Statistically, A4B17 at both 15 mg/kg and 30 mg/kg was more efficacious than enzalutamide in the inhibition of tumor growth (p ≤ 0.0001 compared to p = 0.0240) (Figure 6E). Tumor growth inhibition (%TGI) was calculated to be 24.8% for enzalutamide and 34.4 and 54.5% for A4B17 (15 and 30 mg/kg body weight) respectively. Both A4B17

and enzalutamide were well tolerated in this study and did not cause animal weight loss or other signs of toxicity during the entire experiment (Figure 6F). Quantitative RT-PCR showed that genes whose expression was upregulated by A4B17 in the inhibition of cell proliferation were also upregulated in the tumors with impaired growth in the mouse xenograft experiments (Figure S8). These results identify A4B17 as a more suitable AR antagonist compared to enzalutamide in the tumor growth inhibition studies under androgen deprivation conditions.

DISCUSSION

BAG1L regulates AR action through binding to both the AR C-terminal LBD and the NTD (Cato et al., 2017; Shatkina et al., 2003). We have previously reported that AR binding to chromatin is impaired by BAG1L KO or by a C-terminal BAG1L mutant that is defective in AR binding (Cato et al., 2017). In the present study, we have analyzed how BAG1L controls AR action in the nucleus using SMT that allows individual AR proteins to be imaged in time-lapse and their spatial-temporal trajectories to be recorded in real-time. These studies showed that AR dynamics in the nucleus are enhanced in the absence of BAG1L or when its interaction site with the AR NTD is destroyed, as in the case of BAG1L with C-terminal mutations. The enhanced motility of the AR determined in these studies provides a mechanistic explanation for AR's inefficient chromatin binding in the absence of BAG1L or in the presence of the mutant BAG1L (Cato et al., 2017). We also showed in the SMT studies that the fraction of AR with a slow diffusion coefficient that is synonymous with AR chromatin binding is decreased in the absence of BAG1L or in the presence of the mutant BAG1L.

Using the same BAG1L knockout cell lines employed in the SMT, we showed that the expression of classical androgen response genes, such as *KLK3* and *FKBP5*, as well as androgen-responsive genes involved in oxidative stress and metabolism is impacted by the loss of BAG1L. A small molecule A4B17 that targets BAG1 (Kuznik et al., 2021) also downregulated the expression of DHT-induced ROS gene expression in a similar way as in the BAG1L KO cell line, demonstrating that A4B17 can be used to chemically ablate the action of BAG1. With this background information, we tested the action of A4B17 on the proliferation of several AR-positive cell lines and showed as we have previously reported (Kuznik et al., 2021) that it inhibited the proliferation and viability of AR-positive cell lines. We also showed that A4B17 inhibited the proliferation of ER-positive breast cancer cell lines in agreement with previous findings of BAG1L enhancing ERα action and breast cancer cell growth (Cutress et al., 2003; Kizilboga et al., 2019). Our studies further showed, through the use of an ROS inhibitor, that BAG1L regulatory action on the proliferation of PCa cells is linked to a change in the cell's redox state.

Increased oxidative stress and ROS are traditionally associated with tissue injury, DNA damage or programmed cell death, but they are also known to play a role as intracellular messengers during cell growth and differentiation (Sauer et al., 2001). Oxidative stress also plays a role in prostate carcinogenesis (Shiota et al., 2011) and increased ROS is reported to control cellular energy metabolism and growth (Gough and Cotter, 2011; Sullivan and Chandel, 2014). In our studies, although BAG1L KO or the use of A4B17 downregulated the expression of androgen-induced ROS gene expression involved in cell growth, A4B17 also effectively increased the expression of ROS genes that are involved in cell death. It therefore appears that A4B17 uses a dual mechanism to regulate ROS activity to inhibit the growth of PCa cells.

To understand how targeting BAG1 could affect AR action, we critically examined BAG1L interaction with one of the key domains of the AR (the NTD). We used biophysical approaches combined with mutational analysis to determine how BAG1 regulates the action of the intrinsically disordered AR NTD. We identified as a weak interaction site for BAG1L, a polyalanine stretch in ARτ5 that is distinct from the adjacent WHTLF sequence motif that has previously been reported to interact with regulatory factors to enhance AR activity (Yu et al., 2020). A further proof of the relevance of this region for AR action is a report of a reduced transactivation by a naturally occurring AR mutant in an androgen insensitivity patient with an arginine to serine exchange immediately preceding the polyalanine stretch (Lagarde et al., 2012). A polyproline sequence that we identified in our functional data to contribute to BAG1L action but was not identified in our NMR studies as a direct target of BAG1L has previously been reported to bind the factor SH3LY1 whose expression is correlated with androgen-mediated proliferation and migration of PCa cells (Blessing et al., 2015). A possibility therefore exists that this site may exert an allosteric effect on the BAG1L/ARτ5 action.

We have recently reported that A4B17 attenuated the BAG1L-AR NTD interaction and the proliferation of AR-positive prostate cancer cells (Kuznik et al., 2021). In the present study we showed that A4B17 also

inhibited the growth of AR–positive tumor in mouse xenografts. Although A4B17 functions through the AR NTD, it is as good as (or even slightly better than) the clinically approved AR C-terminal antagonist enzalutamide in decreasing the viability of PCa cells and the growth of prostate tumors under castration conditions. It is important to note that the currently approved and clinically available AR antagonists for PCa therapy all function through the C-terminus of the receptor to inhibit tumor growth (Fujii and Kagechika, 2019). Because these antagonists are no longer effective with time, there is an unmet medical need for the development of inhibitors that target other sites of the receptor. A number of advances have already been made in recent years in the development of such inhibitors. For example, there are inhibitors that bind directly to the AR NTD to inhibit AR action (DeMol et al., 2016; Yan et al., 2021), others cause proteasomal degradation of both the full-length AR and AR-Vs (Ponnusamy et al., 2017, 2019), or bind AR coregulators to inhibit AR action and AR-positive PCa growth (Jin et al., 2017; Welti et al., 2021). However, none of these new compounds has been clinically approved, although a few are in clinical trials. Some have shortcomings in reaching the desired goals in clinical trials and their developments have subsequently been discontinued (Mohler et al., 2021). In light of these findings, it is important to further develop AR N-terminal inhibitors that have other modes of action such as the one described here that disrupts the interaction of the AR NTD with the cochaperone BAG1L (Kuznik et al., 2021). Unlike other reported AR NTD inhibitors, A4B17 does not cause a substantial destabilization of the AR nor does it bind directly to the AR. Instead, it exerts its action possibly through conformational changes at the AR NTD as we have previously shown in fluorescence resonance energy transfer studies (Cato et al., 2017). Comparison of the action of A4B17 and enzalutamide has shown that although they have some shared action in the regulation of expression of distinct genes, A4B17 has additional properties that make it a unique inhibitor. Thus, the further development of this inhibitor and other BAG1L inhibitors holds great promise for the future.

Limitations of the study

Although the A4B17 results reported in this work are encouraging, the high IC_{50} values of this compound suggest the need for caution to be exercised in its further development as a PCa therapeutic. However, we believe it is a good chemical probe that could provide invaluable mechanistic information for the future development of more potent BAG1 inhibitors.

STAR★METHODS

Detailed methods are provided in the online version of this paper and include the following:

- KEY RESOURCES TABLE
- RESOURCE AVAILABILITY
  - Lead contact
  - Material availability
  - Data and code availability
- EXPERIMENTAL MODEL AND SUBJECT DETAILS
  - Cell lines
  - Animals
- METHOD DETAILS
  - Western blot analysis
  - Mammalian-one-hybrid and mammalian-two-hybrid assays
  - Immunofluorescence analysis
  - Cell proliferation assay
  - Reduced 2′7-dichlorofluorescein (DCF) diacetate oxidation assay
  - RNA-sequencing
  - Quantitative RT-PCR experiments
  - Single-molecule tracking analysis
  - NMR
  - Bulk synthesis of 2-(4-fluorophenyl)-5-(trifluoromethyl)-1,3-benzothiazole (A4B17)
  - *In vivo* experiments
- QUANTIFICATION AND STATISTICAL ANALYSIS

SUPPLEMENTAL INFORMATION

Supplemental information can be found online at https://doi.org/10.1016/j.isci.2022.104175.

AUTHOR CONTRIBUTIONS

NCK, VS, IIL, NJ, LY, KN, EAN, JTR, CM-G, ARK, RP, SG, VG, CD, LC, AN, MD and CAC-v-C performed the experiments. ACBC conceived the project. ACBC, CM-G, BK, KN, CW, VG, GUN, SB, MB designed the experiments. ACBC, IIL, KN, MD, CW and GUN wrote the manuscript. All authors reviewed the manuscript.

DECLARATION OF INTERESTS

MB is a consultant to and receives sponsored research support from Novartis. MB serves on the SAB of H3 Biomedicine, Kronos Bio, and GV20 Oncotherapy. LC is currently an employee of Sanofi-Aventis, Boston, USA and IL is currently an employee of Abbvie, North Chicago, IL. All other authors declare they have no competing interests.

REFERENCES

Abildgaard, A.B., Gersing, S.K., Larsen-Ledet, S., Nielsen, S.V., Stein, A., Lindorff-Larsen, K., and Hartmann-Petersen, R. (2020). Co-chaperones in targeting and delivery of misfolded proteins to the 26S proteasome. Biomolecules 10, 1141.

Altenhöfer, S., Radermacher, K.A., Kleikers, P.W., Wingler, K., and Schmidt, H.H. (2015). Evolution of NADPH oxidase inhibitors: selectivity and mechanisms for target engagement. Antioxid. Redox Signal. 23, 406–427.

Alto, L.T., and Terman, J.R. (2018). MICALs. Curr. Biol. 28, R538–R541.

Arosio, P., and Levi, S. (2010). Cytosolic and mitochondrial ferritins in the regulation of cellular iron homeostasis and oxidative damage. Biochim. Biophys. Acta 1800, 783–792.

Basu, H.S., Thompson, T.A., Church, D.R., Clower, C.C., Mehraein-Ghomi, F., Amlong, C.A., Martin, C.T., Woster, P.M., Lindstrom, M.J., and Wilding, G. (2009). A small molecule polyamine oxidase inhibitor blocks androgen-induced oxidative stress and delays prostate cancer progression in the transgenic adenocarcinoma of the mouse prostate model. Cancer Res. 69, 7689–7695.

Bernacki, J.P., and Murphy, R.M. (2011). Length-dependent aggregation of uninterrupted polyalanine peptides. Biochemistry 50, 9200–9211.

Blessing, A.M., Ganesan, S., Rajapakshe, K., Ying Sung, Y., Reddy Bollu, L., Shi, Y., Cheung, E., Coarfa, C., Chang, J.T., McDonnell, D.P., et al. (2015). Identification of a novel coregulator, SH3YL1, that interacts with the androgen receptor N-terminus. Mol. Endocrinol. 29, 1426–1439.

Bracher, A., and Verghese, J. (2015). The nucleotide exchange factors of Hsp70 molecular chaperones. Front. Mol. Biosci. 2, 10.

Briknarova, K., Takayama, S., Brive, L., Havert, M.L., Knee, D.A., Velasco, J., Homma, S., Cabezas, E., Stuart, J., Hoyt, D.W., et al. (2001). Structural analysis of BAG1 cochaperone and its interactions with Hsc70 heat shock protein. Nat. Struct. Biol. 8, 349–352.

Cato, L., Neeb, A., Sharp, A., Buzón, V., Ficarro, S.B., Yang, L., Muhle-Goll, C., Kuznik, N.C., Riisnaes, R., Nava Rodrigues, D., et al. (2017). Development of bag-1L as a therapeutic target in androgen receptor-dependent prostate cancer. Elife 6, e27159.

Coldwell, M.J., DeSchoolmeester, M.L., Fraser, G.A., Pickering, B.M., Packham, G., and Willis, A.E. (2001). The p36 isoform of BAG-1 is translated by internal ribosome entry following heat shock. Oncogene 20, 4095–4100.

Da Costa, C.R., Villadiego, J., Sancho, R., Fontana, X., Packham, G., Nateri, A.S., and Behrens, A. (2010). Bag1-L is a phosphorylation-dependent coactivator of c-Jun during neuronal apoptosis. Mol.Cell Biol. 30, 3842–3852.

Culig, Z., Klocker, H., Bartsch, G., and Hobisch, A. (2002). Androgen receptors in prostate cancer. Endocr. Relat. Cancer 9, 155–170.

Cutress, R.I., Townsend, P.A., Sharp, A., Maison, A., Wood, L., Lee, R., Brimmell, M., Mullee, M.A., Johnson, P.W., Royle, G.T., et al. (2003). The nuclear BAG-1 isoform, BAG-1L, enhances oestrogen-dependent transcription. Oncogene 22, 4973–4982.

Dehm, S.M., Regan, K.M., Schmidt, L.J., and Tindall, D.J. (2007). Selective role of an NH2-terminal WxxLF motif for aberrant androgen receptor activation in androgen depletion independent prostate cancer cells. Cancer Res. 67, 10067–10077.

Demand, J., Alberti, S., Patterson, C., and Höhfeld, J. (2001). Cooperation of a ubiquitin domain protein and an E3 ubiquitin ligase during chaperone/proteasome coupling. Curr. Biol. 11, 1569–1577.

Deng, W., Wang, Y., Zhao, S., Zhang, Y., Chen, Y., Zhao, X., Liu, L., Sun, S., Zhang, L., Ye, B., et al. (2018). MICAL1 facilitates breast cancer cell proliferation via ROS-sensitive ERK/cyclin D pathway. J.Cell Mol. Med. 22, 3108–3118.

Froesch, B.A., Takayama, S., and Reed, J.C. (1998). BAG-1L protein enhances androgen receptor function. J. Biol. Chem. 273, 11660–11666.

Fujii, S., and Kagechika, H. (2019). Androgen receptor modulators: a review of recent patents and reports (2012-2018). Expert Opin. Ther. Pat 29, 439–453.

Galletti, G., Leach, B.I., Lam, L., and Tagawa, S.T. (2017). Mechanisms of resistance to systemic therapy in metastatic castration-resistant prostate cancer. Cancer Treat Rev. 57, 16–27.

Garcia, R.R., Masoodi, K.Z., Pascal, L.E., Nelson, J.B., and Wang, Z. (2014). Growth of LAPC4 prostate cancer xenograft tumor is insensitive to 5α-reductase inhibitor dutasteride. Am. J. Clin. Exp. Urol. 2, 82–91.

Gough, D.R., and Cotter, T.G. (2011). Hydrogen peroxide: a Jekyll and Hyde signalling molecule. Cell Death Dis. *2*, e213.

Gronewold, A., Horn, M., and Neundorf, I. (2018). Design and biological characterization of novel cell-penetrating peptides preferentially targeting cell nuclei and subnuclear regions. Beilstein J. Org. Chem. *14*, 1378–1388.

Gueron, G., De Siervi, A., Ferrando, M., Salierno, M., De Luca, P., Elguero, B., Meiss, R., Navone, N., and Vazquez, E.S. (2009). Critical role of endogenous heme oxygenase 1 as a tuner of the invasive potential of prostate cancer cells. Mol. Cancer Res. *7*, 1745–1755.

Guzmán, C., Bagga, M., Kaur, A., Westermarck, J., and Abankwa, D. (2014). ColonyArea: an ImageJ plugin to automatically quantify colony formation in clonogenic assays. PLoS One *9*, e92444.

Han, W., Gao, S., Barrett, D., Ahmed, M., Han, D., Macoska, J.A., He, H.H., and Cai, C. (2018). Reactivation of androgen receptor-regulated lipid biosynthesis drives the progression of castration-resistant prostate cancer. Oncogene *37*, 710–721.

Hansjosten, I., Rapp, J., Reiner, L., Vatter, R., Fritsch-Decker, S., Peravali, R., Palosaari, T., Joossens, E., Gerloff, K., Macko, P., et al. (2018). Microscopy-based high-throughput assays enable multi-parametric analysis to assess adverse effects of nanomaterials in various cell lines. Arch. Toxicol. *92*, 633–649.

Hantouche, C., Williamson, B., Valinsky, W.C., Solomon, J., Shrier, A., and Young, J.C. (2017). Bag1 co-chaperone promotes TRC8 E3 ligase-dependent degradation of misfolded human ether a go-go-related gene (hERG) potassium channels. J. Biol. Chem. *292*, 2287–2300.

Horzmann, K.A., and Freeman, J.L. (2018). Making waves: new developments in toxicology with the zebrafish. Toxicol. Sci. *163*, 5–12.

Hu, J., Yao, H., Gan, F., Tokarski, A., and Wang, Y. (2012a). Interaction of OKL38 and p53 in regulating mitochondrial structure and function. PLoS One *7*, e43362.

Hu, R., Lu, C., Mostaghel, E.A., Yegnasubramanian, S., Gurel, M., Tannahill, C., Edwards, J., Isaacs, W.B., Nelson, P.S., Bluemn, E., et al. (2012b). Distinct transcriptional programs mediated by the ligand- and uncoupled full-length androgen receptor and its splice variants in castration-resistant prostate cancer. Cancer Res. *72*, 3457–3462.

Huang, D., Li, H., He, Q., Yuan, W., Chen, Z., and Yang, H. (2018). Developmental toxicity of diethylnitrosamine in zebrafish embryos/juveniles related to excessive oxidative stress. Water Air Soil Pollut. *229*, 81.

Irfan, A., Batool, F., Zahra Naqvi, S.A., Islam, A., Osman, S.M., Nocentini, A., Alissa, S.A., and Supuran, C.T. (2020). Benzothiazole derivatives as anticancer agents. J. Enzym. Inhib. Med. Chem. *35*, 265–279.

Jin, L., Garcia, J., Chan, E., de la Cruz, C., Segal, E., Merchant, M., Kharbanda, S., Raisner, R., Haverty, P.M., Modrusan, Z., et al. (2017). Therapeutic targeting of the CBP/p300 bromodomain blocks the growth of castration-resistant prostate cancer. Cancer Res. *77*, 5564–5575.

Jodoin, R., Carrier, J.C., Rivard, N., Bisaillon, M., and Perreault, J.P. (2019). G-quadruplex located in the 5′UTR of the BAG-1 mRNA affects both its cap-dependent and cap-independent translation through global secondary structure maintenance. Nucleic Acids Res. *47*, 10247–10266.

Kassel, O., Schneider, S., Heilbock, C., Litfin, M., Gottlicher, M., and Herrlich, P. (2004). A nuclear isoform of the focal adhesion LIM-domain protein Trip6 integrates activating and repressing signals at AP-1- and NF-kappaB-regulated promoters. Genes Dev. *18*, 2518–2528.

Kimmel, C.B., Ballard, W.W., Kimmel, S.R., Ullmann, B., and Schilling, T.F. (1995). Stages of embryonic development of the zebrafish. Dev. Dyn. *203*, 253–310.

Kizilboga, T., Baskale, E.A., Yildiz, J., Akcay, I.M., Zemheri, E., Can, N.D., Ozden, C., Demir, S., Ezberci, F., and Dinler-Doganay, G. (2019). Bag-1 stimulates bad phosphorylation through activation of Akt and Raf kinases to mediate cell survival in breast cancer. BMC Cancer *19*, 1254.

Klee, E.W., Bondar, O.P., Goodmanson, M.K., Dyer, R.B., Erdogan, S., Bergstralh, E.J., Bergen, H.R., 3rd, Sebo, T.J., and Klee, G.G. (2012). Candidate serum biomarkers for prostate adenocarcinoma identified by mRNA differences in prostate tissue and verified with protein measurements in tissue and blood. Clin. Chem. *58*, 599–609.

Klein, K.A., Reiter, R.E., Redula, J., Moradi, H., Zhu, X.L., Brothman, A.R., Lamb, D.J., Marcelli, M., Belldegrun, A., Witte, O.N., et al. (1997). Progression of metastatic human prostate cancer to androgen independence in immunodeficient SCID mice. Nat. Med. *3*, 402–408.

Kuznik, N.C., Solozobova, V., Jung, N., Gräßle, S., Lei, Q., Lewandowski, E.M., Munganti, R., Zoubeidi, A., Chen, Y., Bräse, S., et al. (2021). Development of a benzothiazole scaffold-based androgen receptor n-terminal inhibitor for treating androgen-responsive prostate cancer. ACS Chem. Biol. *16*, 2103–2108.

Lagarde, W.H., Blackwelder, A.J., Minges, J.T., Hnat, A.T., French, F.S., and Wilson, E.M. (2012). Androgen receptor exon 1 mutation causes androgen insensitivity by creating phosphorylation site and inhibiting melanoma antigen-A11 activation of NH2- and carboxyl-terminal interaction-dependent transactivation. J. Biol. Chem. *287*, 10905–10915.

Lee, I.I., Kuznik, N.C., Rottenberg, J.T., Brown, M., and Cato, A.C.B. (2019). BAG1L: a promising therapeutic target for androgen receptor-dependent prostate cancer. J. Mol. Endocrinol. *62*, R289–R299.

Li, S., Zhuang, Z., Wu, T., Lin, J.C., Liu, Z.X., Zhou, L.F., Dai, T., Lu, L., and Ju, H.Q. (2018). Nicotinamide nucleotide transhydrogenase-mediated redox homeostasis promotes tumor growth and metastasis in gastric cancer. Redox Biol. *18*, 246–255.

Li, Y., Chan, S.C., Brand, L.J., Hwang, T.H., Silverstein, K.A., and Dehm, S.M. (2013a). Androgen receptor splice variants mediate enzalutamide resistance in castration-resistant prostate cancer cell lines. Cancer Res. *73*, 483–489.

Li, Y., Ishitsuka, Y., Hedde, P.N., and Nienhaus, G.U. (2013b). Fast and efficient molecule detection in localization-based super-resolution microscopy by parallel adaptive histogram equalization. ACS Nano *7*, 5207–5214.

Li, Y., Shang, L., and Nienhaus, G.U. (2016). Super-resolution imaging-based single particle tracking reveals dynamics of nanoparticle internalization by live cells. Nanoscale *8*, 7423–7429.

Liberzon, A., Subramanian, A., Pinchback, R., Thorvaldsdóttir, H., Tamayo, P., and Mesirov, J.P. (2011). Molecular signatures database (MSigDB) 3.0. Bioinformatics *27*, 1739–1740.

Love, M.I., Huber, W., and Anders, S. (2014). Moderated estimation of fold change and dispersion for RNA-seq data with DESeq2. Genome Biol *15*, 550.

Manley, S., Gillette, J.M., Patterson, G.H., Shroff, H., Hess, H.F., Betzig, E., and Lippincott-Schwartz, J. (2008). High-density mapping of single-molecule trajectories with photoactivated localization microscopy. Nat. Methods *5*, 155–157.

Marcias, G., Erdmann, E., Lapouge, G., Siebert, C., Barthélémy, P., Duclos, B., Bergerat, J.P., Céraline, J., and Kurtz, J.E. (2010). Identification of novel truncated androgen receptor (AR) mutants including unreported pre-mRNA splicing variants in the 22Rv1 hormone-refractory prostate cancer (PCa) cell line. Hum. Mutat. *31*, 74–80.

McEwan, I.J. (2012). Intrinsic disorder in the androgen receptor: identification, characterisation and drugability. Mol. Biosyst. *8*, 82–90.

Melong, N., Steele, S., MacDonald, M., Holly, A., Collins, C.C., Zoubeidi, A., Berman, J.N., and Dellaire, G. (2017). Enzalutamide inhibits testosterone-induced growth of human prostate cancer xenografts in zebrafish and can induce bradycardia. Sci. Rep. *7*, 14698.

Mink, S., Kerber, U., and Klempnauer, K.H. (1996). Interaction of C/EBPbeta and v-Myb is required for synergistic activation of the mim-1 gene. Mol.Cell Biol. *16*, 1316–1325.

Mohler, M.L., Sikdar, A., Ponnusamy, S., Hwang, D.J., He, Y., Miller, D.D., and Narayanan, R. (2021). An overview of next-generation androgen receptor-targeted therapeutics in development for the treatment of prostate cancer. Int. J. Mol. Sci. *22*, 2124.

De Mol, E., Fenwick, R.B., Phang, C.T., Buzón, V., Szulc, E., de la Fuente, A., Escobedo, A., García, J., Bertoncini, C.W., Estébanez-Perpiñá, E., et al. (2016). EPI-001, a compound active against castration-resistant prostate cancer, targets transactivation unit 5 of the androgen receptor. ACS Chem. Biol. *11*, 2499–2505.

Mootha, V.K., Lindgren, C.M., Eriksson, K.F., Subramanian, A., Sihag, S., Lehar, J., Puigserver, P., Carlsson, E., Ridderstråle, M., Laurila, E., et al. (2003). PGC-1alpha-responsive genes involved in oxidative phosphorylation are coordinately

downregulated in human diabetes. Nat. Genet. *34*, 267–273.

Nguyen, P., Hess, K., Smulders, L., Le, D., Briseno, C., Chavez, C.M., and Nikolaidis, N. (2020). Origin and evolution of the human Bcl2-associated athanogene-1 (BAG-1). Int. J. Mol. Sci. *21*, 9701.

Nienhaus, G.U., Nienhaus, K., Hölzle, A., Ivanchenko, S., Renzi, F., Oswald, F., Wolff, M., Schmitt, F., Röcker, C., Vallone, B., et al. (2006). Photoconvertible fluorescent protein EosFP: biophysical properties and cell biology applications. Photochem. Photobiol. *82*, 351–358.

O'Donnell, V.B., Smith, G.C., and Jones, O.T. (1994). Involvement of phenyl radicals in iodonium inhibition of flavoenzymes. Mol. Pharmacol. *46*, 778–785.

Ponnusamy, S., Coss, C.C., Thiyagarajan, T., Watts, K., Hwang, D.J., He, Y., Selth, L.A., McEwan, I.J., Duke, C.B., Pagadala, J., et al. (2017). Novel selective agents for the degradation of androgen receptor variants to treat castration-resistant prostate cancer. Cancer Res. *77*, 6282–6298.

Ponnusamy, S., He, Y., Hwang, D.J., Thiyagarajan, T., Houtman, R., Bocharova, V., Sumpter, B.G., Fernandez, E., Johnson, D., Du, Z., et al. (2019). Orally bioavailable androgen receptor degrader, potential next-generation therapeutic for enzalutamide-resistant prostate cancer. Clin.Cancer Res. *25*, 6764–6780.

Ripple, M.O., Henry, W.F., Rago, R.P., and Wilding, G. (1997). Prooxidant-antioxidant shift induced by androgen treatment of human prostate carcinoma cells. J. Natl. Cancer Inst. *89*, 40–48.

Van Royen, M.E., van Cappellen, W.A., Geverts, B., Schmidt, T., Houtsmuller, A.B., and Schaaf, M.J. (2014). Androgen receptor complexes probe DNA for recognition sequences by short random interactions. J.Cell Sci. *127*, 1406–1416.

Sauer, H., Wartenberg, M., and Hescheler, J. (2001). Reactive oxygen species as intracellular messengers during cell growth and differentiation. Cell. Physiol. Biochem. *11*, 173–186.

Schweizer, M.T., Haugk, K., McKiernan, J.S., Gulati, R., Cheng, H.H., Maes, J.L., Dumpit, R.F., Nelson, P.S., Montgomery, B., McCune, J.S., et al. (2018). A phase I study of niclosamide in combination with enzalutamide in men with castration-resistant prostate cancer. PLoS One *13*, e0198389.

Sharp, A., Crabb, S.J., Townsend, P.A., Cutress, R.I., Brimmell, M., Wang, X.H., and Packham, G. (2004). BAG-1 in carcinogenesis. Expert Rev. Mol. Med. *6*, 1–15.

Shatkina, L., Mink, S., Rogatsch, H., Klocker, H., Langer, G., Nestl, A., and Cato, A.C. (2003). The cochaperone Bag-1L enhances androgen receptor action via interaction with the NH2-terminal region of the receptor. Mol.Cell Biol. *23*, 7189–7197.

Shiota, M., Yokomizo, A., and Naito, S. (2011). Oxidative stress and androgen receptor signaling in the development and progression of castration-resistant prostate cancer. Free Radic. Biol. Med. *51*, 1320–1328.

Sondermann, H., Scheufler, C., Schneider, C., Hohfeld, J., Hartl, F.U., and Moarefi, I. (2001). Structure of a Bag/Hsc70 complex: convergent functional evolution of Hsp70 nucleotide exchange factors. Science *291*, 1553–1557.

Subramanian, A., Tamayo, P., Mootha, V.K., Mukherjee, S., Ebert, B.L., Gillette, M.A., Paulovich, A., Pomeroy, S.L., Golub, T.R., Lander, E.S., et al. (2005). Gene set enrichment analysis: a knowledge-based approach for interpreting genome-wide expression profiles. Proc. Natl. Acad. Sci. U S A *102*, 15545–15550.

Sullivan, L.B., and Chandel, N.S. (2014). Mitochondrial reactive oxygen species and cancer. Cancer Metab. *2*, 17.

Takayama, S., Krajewski, S., Krajewska, M., Kitada, S., Zapata, J.M., Kochel, K., Knee, D., Scudiero, D., Tudor, G., Miller, G.J., et al. (1998). Expression and location of Hsp70/Hsc-binding anti-apoptotic protein BAG-1 and its variants in normal tissues and tumor cell lines. Cancer Res. *58*, 3116–3131.

Tsai, C.H., Shen, Y.C., Chen, H.W., Liu, K.L., Chang, J.W., Chen, P.Y., Lin, C.Y., Yao, H.T., and Li, C.C. (2017). Docosahexaenoic acid increases the expression of oxidative stress-induced growth inhibitor 1 through the PI3K/Akt/Nrf2 signaling pathway in breast cancer cells. Food Chem. Toxicol. *108*, 276–288.

Veldscholte, J., Ris-Stalpers, C., Kuiper, G.G., Jenster, G., Berrevoets, C., Claassen, E., van Rooij, H.C., Trapman, J., Brinkmann, A.O., and Mulder, E. (1990). A mutation in the ligand binding domain of the androgen receptor of human LNCaP cells affects steroid binding characteristics and response to anti-androgens. Biochem. Biophys. Res. Commun. *173*, 534–540.

Ware, K.E., Garcia-Blanco, M.A., Armstrong, A.J., and Dehm, S.M. (2014). Biologic and clinical significance of androgen receptor variants in castration resistant prostate cancer. Endocr. Relat. Cancer *21*, T87–T103.

Welti, J., Sharp, A., Brooks, N., Yuan, W., McNair, C., Chand, S.N., Pal, A., Figueiredo, I., Riisnaes, R., Gurel, B., et al. (2021). Targeting the p300/CBP axis in lethal prostate cancer. Cancer Discov. *11*, 1118–1137.

Yan, L., Banuelos, C.A., Mawji, N.R., Patrick, B.O., Sadar, M.D., and Andersen, R.J. (2021). Structure-activity relationships for the marine natural product sintokamides: androgen receptor N-terminus antagonists of interest for treatment of metastatic castration-resistant prostate cancer. J. Nat. Prod. *84*, 797–813.

Yang, X., Chernenko, G., Hao, Y., Ding, Z., Pater, M.M., Pater, A., and Tang, S.C. (1998). Human BAG-1/RAP46 protein is generated as four iso-forms by alternative translation initiation and overexpressed in cancer cells. Oncogene *17*, 981–989.

Yu, X., Yi, P., Hamilton, R.A., Shen, H., Chen, M., Foulds, C.E., Mancini, M.A., Ludtke, S.J., Wang, Z., and O'Malley, B.W. (2020). Structural insights of transcriptionally active, full-length androgen receptor coactivator complexes. Mol.Cell *79*, 812–823.

Yuan, F., Hankey, W., Wu, D., Wang, H., Somarelli, J., Armstrong, A.J., Huang, J., Chen, Z., and Wang, Q. (2019). Molecular determinants for enzalutamide-induced transcription in prostate cancer. Nucleic Acids Res. *47*, 10104–10114.

Zadra, G., Ribeiro, C.F., Chetta, P., Ho, Y., Cacciatore, S., Gao, X., Syamala, S., Bango, C., Photopoulos, C., Huang, Y., et al. (2019). Inhibition of de novo lipogenesis targets androgen receptor signaling in castration-resistant prostate cancer. Proc. Natl. Acad. Sci. U S A *116*, 631–640.

Zegarra-Moro, O.L., Schmidt, L.J., Huang, H., and Tindall, D.J. (2002). Disruption of androgen receptor function inhibits proliferation of androgen-refractory prostate cancer cells. Cancer Res. *62*, 1008–1013.

STAR★METHODS

KEY RESOURCES TABLE

REAGENT or RESOURCE	SOURCE	IDENTIFIER
Antibodies		
anti-Androgen Receptor (441)	Santa Cruz	Cat# sc-7305; RRID:AB_626671
anti-BAG1 (CC9E8)	Santa Cruz	Cat# sc-33704; RRID:AB_626720
anti-β-actin	Santa Cruz	Cat# sc-47778; RRID:AB_626632
Bacterial and virus strains		
E. coli strain BL21 (DE3)	Invitrogen	Cat# EC0114
E. coli strain DH5α	Invitrogen	Cat# EC0112
Chemicals, peptides, and recombinant proteins		
(FITC-VQRKRQKLMPGLRK RLRKFRNKKLENPLD YGSAWAAAAAQCRY)	Peptide 2.0 Inc	N/A
Control FITC-labeled NLS-CPP peptide	Peptide 2.0 Inc	N/A
(Dulbecco's Modified Eagle's Medium) DMEM	Gibco	Cat# 41966-029
RPMI 1640 ●Without phenol red	Gibco	Cat# 11875-085 Cat# 11835030
Fetal Bovine Serum (FBS)	Gibco	Cat# 10270-106
5α-Androstan-17β-ol-3-on (Dihydrotestosterone)	Merck AG	Cat# A8380
Penicillin- Streptomycin	Gibco	Cat# 15140122
L-glutamine	Gibco	Cat# 25030081
Fish water 60 μg/mL f.c. sea salts	Instant Ocean Spectrum Brands	Cat# SS15-10
Dimethyl sulfoxide	Carl Roth	Cat# A994.2
Passive lysis buffer	Promega	Cat# E1941
FuGENE HD	Promega	Cat# E2311
Dulbecco's PBS	Gibco	Cat# 14190094
Glyglycin	Carl Roth	Cat# 3794.4
Magnesium sulfate heptahydrate	Carl Roth	Cat# P027.1
1,4-Dithiothreitol	Carl Roth	Cat# 6908.2
Adenosine-5′-triphosphate-disodium salt	Carl Roth	Cat# HN35.2
D-Luciferin Firefly	Biosynth/Carbosynth	Cat# L-8200
EGTA	Carl Roth	Cat# 3054.1
Potassium dihydrogen phosphate	Carl Roth	Cat# P018.1
Di-potassium hydrogen phosphate	Carl Roth	Cat# P749.1
Sodium chloride	Carl Roth	Cat# 3957.2
EDTA disodium salt dihydrate	Carl Roth	Cat# 8043.1
Coelenterazine	Biosynth/Carbosynth	Cat# C-7002
Hoechst stain 33,258	Abcam	Cat# ab228550
Hoechst stain 33,342	Invitrogen	Cat# 62249
3-(4,5-dimethylthiazol-2-yl)-2, 5-diphenyltetrazolium bromide (MTT)	Sigma-Aldrich	Cat# 1.11714
2-propanol	Carl Roth	Cat# 9866.1

Continued

REAGENT or RESOURCE	SOURCE	IDENTIFIER
Crystal Violet	SERVA	Cat# 27335.01
Methanol	Carl Roth	Cat# 8388.3
2′7-dichlorofluorescein diacetate	Thermo Fisher	Cat# D399
R1881 (Metribolone)	Sigma-Aldrich	Cat# R0908
Enzalutamide (MDV3100)	Selleckchem	Cat# S1250
Ammonium Chloride (15N)	Cambridge Isotope Laboratories	Cat# NLM-467-10
2-amino-4-(trifluoromethyl)benzenethiol; hydron; chloride	Sigma-Aldrich	Cat# 365734
4-fluorobenzoyl chloride	Sigma-Aldrich	Cat# 119946
Dioxane	Fisher Scientific	Cat# 10141470
methylene chloride	Fisher Scientific	Cat# 10616642
$NaHCO_3$	Fisher Scientific	Cat# 10553325
Na_2SO_4	Fisher Scientific	Cat# 10032590
Celite	Fisher Scientific	Cat# 10316691
Cyclohexane	VWR	Cat# 23224.327
ethyl acetate	VWR	Cat# 23882.330
Silica gel	Interchim	Cat# OV004A
corn oil	Sigma Aldrich	Cat# C8267
Matrigel	Corning	Cat# 354248
Critical commercial assays		
Venor®GeM Classic Mycoplasma Detection Kit	Minerva Biolabs	Cat# 11-1250
InnuPrep RNA Mini Kit 2	Analytik Jena	Cat# 845-KS-2040250
NEBNext® UltraTM RNA Library Prep Kit	New England Biolabs	Cat# E7530L
PE Cluster Kit cBot-HS	Illumina - Novogene	
M-MLV Reverse Transcriptase	Promega	Cat# M1701
SYBR Green GoTaq PCR mix	Promega	Cat# A6002
Deposited data		
The RNA-seq data deposited at the GEO repository	Cato et al. (2017)	GSE89939
	This study	GSE159606
	This study	GSE182278
Experimental models: Cell lines		
LNCaP	ATCC	Cat# CRL-1740
LNCaP-95	Hu et al. (2012b)	
LAPC-4	ATCC	Cat# CRL-13009
HeLa	ATCC	Cat# CCL-2
MCF-7	ATCC	Cat# HTB-22
ZR75-1	ATCC	Cat# CRL-1500
MDA-MB-231	ATCC	Cat# HTB-26
LNCaP control and BAG1LKO cells	Cato et al. (2017)	
Experimental models: Organisms/strains		
Zebrafish wild-type AB strain	EZRC	#1175
Male athymic nude-Foxn1[nu] mice	Envigo	#6901M
Oligonucleotides		
Rib36B4 For	5′-CTCCTGAGCGCAAGTACTCC-3′	Metabion
Rib36B4 Rev	5′-GTCACCTTCACCGTTGTTCCA-3′	Metabion

Continued

REAGENT or RESOURCE	SOURCE	IDENTIFIER
KLK3 For	5′-CCCGGTTGTCTTCCTCACCC-3′	Metabion
KLK3 Rev	5′-GCCTCCCACAATCCGAGACA-3′	Metabion
F5 For	5′-TCCAGGCCGAGAATACACCTA-3′	Metabion
F5 Rev	5′-CGATTTGCTTGTCAAACGTCTTC-3′	Metabion
DUOX1 For	5′-GTGCTCCCTCTGTTGTTCGT-3′	Metabion
DUOX1 Rev	5′-GCTTCTCAGACACGATGCTCT-3′	Metabion
MICAL1 For	5′-ATGGGCAGCCTGATGTCTCT-3′	Metabion
MICAL1 Rev	5′-GGCGCCATGCTTCTCTTG-3′	Metabion
NNT For	5′-TGGTCAAGCAGGGTTTTAATGT-3′	Metabion
NNT Rev	5′-TCCTTTGCCCCTTGGATTTGG-3′	Metabion
BAG1 For	5′-GGTGACCAGGGAGGAAATGG-3′	Metabion
BAG1 Rev	5′-GTGCTGACAACGGTGTTTCC-3′	Metabion
AR For	5′-AGCGACTTCACCGCACCT-3′	Metabion
AR Rev	5′-GTTTCCCTTCAGCGGCTCTTT-3′	Metabion
FKBP5 For	5′-TTCAAGGGAGGCAAATACATG-3′	Metabion
FKBP5 Rev	5′-TCCAAGGGCCTTGTCACAG-3′	Metabion
SLC7A11 For	5′-ATGCAGTGGCAGTGACCTTT-3′	Metabion
SLC7A11 Rev	5′-CATGGAGCCAAAGCAGGAGA-3′	Metabion
HMOX1 For	5′-ACTGCGTTCCTGCTCAACAT-3′	Metabion
HMOX1 Rev	5′-GGGGCAGAATCTTGCACTTT-3′	Metabion
S100P For	5′-CATGGGCATGATCATAGACGTCTTTT-3′	Metabion
S100P Rev	5′-AATTTATCCACGGCATCCTTGTCTTTT-3′	Metabion
FTH1 For	5′-CGCCAGAACTACCACCAG-3′	Metabion
FTH1 Rev	5′-TTCAAAGCCACATCATCG-3′	Metabion
OSGIN For	5′-AGAAGAAGCGAAGAGGTC-3′	Metabion
OSGIN Rev	5′-CGGACACAAAGTTATGCC-3′	Metabion
Recombinant DNA		
pG5 ΔE4 luc	Mink et al. (1996)	
Ubi-Renilla luciferase	Kassel et al. (2004)	
pM AR τ5	Shatkina et al. (2003)	
pcDNA3.1	Thermo Fisher	Cat# V79020
pcDNA3.1 BAG1L	Froesch et al., 1998	
VP-16	Clontech	Cat# 630305
VP-16 BAG1L	Katia Jehle	N/A
AR-mEos2	Emmanuel Oppong	N/A
Software and algorithms		
ImageJ		https://imagej.nih.gov/ij/download.html
ColonyArea	Guzmán et al. (2014)	
GraphPad Prism8	GraphPad	https://www.graphpad.com/
SoftMax Pro 7	Molecular Devices	
GSEA Software v4.1.0	Mootha et al. (2003); Subramanian et al. (2005)	http://www.gsea-msigdb.org/ gsea/login.jsp;jsessionid=3B86CA47 2E2D1D71844F8EC8F4872140
Image Lab	Bio-Rad	https://www.bio-rad.com/de-de/product/ image-lab-software?ID=KRE6P5E8Z

RESOURCE AVAILABILITY

Lead contact

Further information and requests for resources and reagents should be directed to and will be fulfilled by the lead Contact, Andrew C. B. Cato (andrew.cato@kit.edu).

Material availability

This study generated a small molecular inhibitor, A4B17, targeting the BAG1-AR interaction. The material will be available for academic researchers upon completion of the Material Transfer Agreement.

Data and code availability

- The RNA-seq data is deposited at the GEO repository under accession number GEO:GSE89939, GEO:GSE159606 and GEO:GSE182278.

- This paper does not report original code.

- Any additional information required to reanalyze the reported data is available from the Lead contact upon request.

EXPERIMENTAL MODEL AND SUBJECT DETAILS

Cell lines

Unless otherwise stated, all cell lines were obtained from the AmericanType Culture Collection and their identities were confirmed by short tandem repeat profiling (BioSynthesis, Lewisville, TX and DSMZ Braunschweig, Germany). LNCaP95 was generously provided by Steve Plymate (Seattle, USA). All cell lines were confirmed to be mycoplasma negative, using the VenorGeM Classic Mycoplasma Detection Kit for conventional PCR (Minerva Biolabs, Berlin, Germany). HeLa cells were cultured in DMEM (Gibco, Thermo Fisher, Frankfurt, Germany) supplemented with 10% fetal bovine serum (FBS) (Gibco, Thermo Fisher, Frankfurt, Germany). All other cell lines and parental LNCaP, LAPC-4, MCF-7, ZR75-1 and MDA-MB-231 cells were cultured in RPMI 1640 medium (Gibco, Thermo Fisher, Frankfurt, Germany) supplemented with 10% FBS (Gibco, Thermo Fisher, Frankfurt, Germany). LAPC-4 cells were additionally supplemented with 1 nM dihydrotestosterone (DHT) (Merck, Darmstadt, Germany). Unless otherwise stated, for experiments requiring hormone starvation, cells were cultured for 72 h in phenol red-free RPMI 1640 medium, supplemented with 3% charcoal-stripped fetal calf serum (CCS). LNCaP95 cells were cultured in phenol red-free RPMI 1640 supplemented with 10% CCS, penicillin (100 u/mL), streptomycin (100 u/mL), and L-glutamine (2 mM) (Gibco, Thermo Fisher, Frankfurt, Germany). LNCaP TALEN BAG1L KO and vector controls are described in Cato et al. (2017).

Animals

All experiments were performed according to European and German statutory regulations and approved by the Regierungspräsidium Karlsruhe, Germany.

Zebrafish

Zebrafish of the wild-type AB strain (EZRC, Karlsruhe, Germany) were maintained according to standard procedures. The fish were kept at a constant temperature ($28 \pm 1°C$) and under a 14–10 h light-dark cycle. They were fed twice a day, once with dry food and once with live artemia. The health of the fish was monitored by visual inspection.

For breeding, adult male and female fish were separated the night before fertilization and allowed to mate the following morning in standard breeding cages. Zebrafish embryos were collected using standard fish nets and incubated in fish water (60 µg/mL f.c. sea salts Instant Ocean Spectrum Brands, Blacksburg, VA) at 28°C.

Mice

Male athymic nude-Foxn1[nu] mice (6–7 weeks old) were purchased from Envigo RMS GmbH (Düsseldorf, Germany), maintained in a temperature-controlled room with a 12 h/12 h light/dark schedule, and fed *ad libitum*.

METHOD DETAILS

Western blot analysis

Control and BAG1L KO LNCaP cells, as well as 22Rv.1 cells (0.5×10^6 cells) were seeded in 10 cm^2 plates. Cells were treated with indicated concentrations of A4B17 or DMSO and incubated for 48hat 48 h at 37°C. Cells were harvested in 1x Passive lysis buffer, frozen at -80°C for 10 min and sonicated. Equal amounts of whole cell lysate were analyzed by sodium dodecyl PAGE.

Mammalian-one-hybrid and mammalian-two-hybrid assays

HeLa cells were seeded at a density of 2×10^5 cells per well in 6-well plates. For all reporter gene assays the following plasmids were used: pG5 ΔE4 luc (0.8 μg), renilla luciferase (0.2 μg), pM AR τ5 wild-type (Shatkina et al., 2003) or mutants (0.2 μg). In mammalian-one-hybrid assays, pcDNA3.1 empty vector or pcDNA3.1 BAG1L (1 μg, kind gift from J. Reed) was additionally transfected to the above reaction mixture. In mammalian-two-hybrid assays, a VP-16 (kind gift from Karin Knudsen) or VP-16 BAG1L (1 μg) was used instead. The VP-16 BAG1L plasmid was constructed by restriction enzyme digestion of the plasmid pcDNA3VP16-ΔOCCR and pGex-BAG1L with BamHI and XbaI and subsequent ligation of the BAG1L fragment to the pcDNA3VP16 vector.

Plasmid DNA was diluted with serum-free medium (Gibco, Thermo Fisher, Frankfurt, Germany) containing 4.4 μL of FuGENE HD (Promega, Walldorf, Germany) to a final volume of 100 μL. The solution was gently mixed by inversion and incubated for 15 min at room temperature and was afterward added dropwise to the cell culture medium. Cells were harvested 48 h post transfection after washing once with 1x PBS (-MgCl$_2$/-CaCl$_2$; Gibco, Thermo Fisher, Frankfurt, Germany) and addition of 200 μL 1x Passive lysis buffer (Promega, Walldorf, Germany). For each sample, firefly and renilla luciferase activity was measured in duplicates with 20 μL of lysates in a 96-well luminometer plate. For the measurement of the firefly-luciferase activity 70 μL of Gly-Gly-Buffer (25 mM Glyglycin, 15 mM MgSO4, 1 mM DTT and 0.1 mM ATP) and 20 μL of luciferin solution (1 mM firefly luciferin, 25 mM Glyglycin, 15 mM MgSO4, 4 mM EGTA) were autoinjected per well and the luciferase activity was measured in a Victor Light 1420 Luminescence Counter (PerkinElmer, Rodau, Deutschland). For the measurement of renilla luciferase activity, 100 μL of Coelenterazin buffer (0.1 M KPi (0.2 M KH2PO4, 0.2 M K2HPO4), 0.5 M NaCl, 1 mM EDTA, pH 7.6, 0.2 nM Coelenterazin) was added and processed in a similar way as the firefly-luciferase. The relative luciferase activity was calculated by dividing firefly-luciferase activity with renilla-luciferase activity.

Immunofluorescence analysis

For cellular peptide uptake studies, a FITC-labeled peptide was used that consisted of the BAG1L interaction sequence (AR 385-405) tagged with a NLS and a CPP sequence (N50-sC18*) (Gronewold et al., 2018)

(FITC-VQRKRQKLMPGLRKRLRKFRNKKLENPLDYGSAWAAAAAQCRY) or a FITC-labeled NLS-CPP peptide as control. The peptides (synthesized by Peptide 2.0 Inc. Chantilly VA USA) were dissolved in DMSO (Carl Roth, Karlsruhe, Germany) and administered at 10 μM in serum-free medium for 20 min. LNCaP and LNCaP95 cells were serum-starved for 72 h before peptide addition. Thereafter, the peptides were removed and cells were further cultured in their respective culture media for 1 h before treatment with 10 nM DHT for 17 h for LNCaP cells, or 7 h for LNCaP95. RNA was prepared using the InnuPrep RNA Mini Kit 2.0 (Analytik Jena, Jena, Germany) according to manufacturer protocol and qRT-PCR analyses were carried out. For microscopy studies, 10 μg/mL Hoechst stain 33342 (Invitrogen, Carlsbad, USA) was added after the 20 min peptide treatment to identify the nuclei. Fluorescence images were taken using a confocal laser scanning system (Zeiss LSM800).

Cell proliferation assay

MTT cell viability assay

Cells were seeded in duplicates at a density of 10^4 cells/well in a 24-well plate format and incubated for 6 days in culture medium. Thereafter, the medium was exchanged for a fresh medium containing 0.5 mg/mL MTT (3-(4,5-dimethylthiazol-2-yl)-2,5-diphenyltetrazolium bromide) (Sigma-Aldrich, Darmstadt, Germany) and incubated at 37°C for 2 h until intracellular purple formazan crystals were formed. The MTT solution was removed and the purple crystals were dissolved in isopropanol (Carl Roth, Karlsruhe, Germany) and the optical absorbance at 590 nm was recorded using SpectraMax iD3 (Molecular Devices, San Jose, CA, USA).

Clonogenic assay

Cells were seeded at a density of 2×10^3 cells/well in RPMI 1640 supplemented with 10% FBS, penicillin (100 u/mL), streptomycin (100 u/mL), and L-glutamine (2 mM) (Gibco, Thermo Fischer, Frankfurt, Germany). Cells were treated with increasing concentrations of A4B17 and cultured for 14 days. Medium and compounds were exchanged after 7 days. The formation of colonies was visualized using 0.5% crystal violet (w/v) (SERVA, Heidelberg, Germany) in 20% methanol (v/v) (Carl Roth, Karlsruhe, Germany). Plates were scanned in a conventional office scanner (Epson, Meerbusch, Germany). The area covered by colonies was calculated using the ColonyArea Plugin for ImageJ (Guzmán et al., 2014).

Reduced 2′7-dichlorofluorescein (DCF) diacetate oxidation assay

DCF assay was carried out essentially as described by Ripple et al. (1997). LNCaP control and BAG1L KO cells were cultured 2 days in phenol red-free RPMI medium supplemented with 4% CCS and 1% FCS (Gibco, Thermo Fischer, Frankfurt, Germany). Thereafter the cells were plated at 1.5×10^4 cells in 96 well plates in phenol red-free RPMI medium supplemented with 5% CCS and treated with 10^{-8} M R1881 (Sigma-Aldrich) for 96 h.

Cells were loaded with 10 μM H2DCF-DA (Thermo Fisher Scientific, Karlsruhe, Germany) in phenol red-free medium for 40 min. Cells were subsequently washed with medium and further incubated in medium for 120 min at room temperature before analysis of fluorescence at 485 nm excitation and 530 nm emission using a multi-well fluorescence reader (SpectraMax iD3, Molecular Devices with SoftMax Pro 7 software, Biberach an der Riss, Germany). After the DCF assay, cell nuclei were stained with a Hoechst dye (0.3 μg/mL final concentration) for 30 min and imaged using an automated fluorescence microscope (IX81, Olympus, Germany) as described in Hansjosten et al. (2018) (Hansjosten et al., 2018). Cell numbers were determined with the image analysis software scan^R (Olympus, Germany) using the Edge Segmentation module.

For analysis of the effect of A4B17 on ROS production, 1×10^4 LNCaP cells were seeded in 96 well plates in phenol red-free RPMI 1640 medium supplemented with 4% CCS and 1% FBS. After 24 h, medium was changed to phenol red-free RPMI 1640 medium supplemented with 5% CCS and cells were exposed to DMSO, 1 μM or 10 μM A4B17. After 24 h preincubation with the compounds, 10^{-8} M R1881 or ethanol was added to the cells for 72 h. Cells were loaded with 10 μM H2DCF-DA (Thermo Fisher Scientific, Karlsruhe, Germany) in phenol red-free medium for 40 min, subsequently washed with medium and further incubated in medium for 120 min at 37°C before analysis of fluorescence and further processing as described above.

RNA-sequencing

RNA-seq studies with BAG1L control and KO LNCaP cells have previously been described (Cato et al., 2017). RNA-seq results on AR target genes in BAG1L KO cells were defined as genes with DHT-induced differential expression (p(FDR)≤0.05, fold change ≥1.5).

RNA-seq studies with control and A4B17 treated LNCaP cells were performed with hormone-starved LNCaP cells treated with 10 nM DHT in the absence and presence of 10 μM A4B17 for 16 h. RNA was extracted using innuPREP RNA mini Kit 2.0 (Analytic Jena, Germany). Sequencing libraries were generated using NEBNext® UltraTM RNA Library Prep Kit for Illumina® (NEB, Ipswich, MA, USA) following manufacturer's recommendations and index codes were added to attribute sequences to each sample. The clustering of the index-coded samples was performed on a cBot Cluster Generation System using PE Cluster Kit cBot-HS (Illumina, San Diego, CA, USA) according to the manufacturer's instructions. After cluster generation, the library preparations were sequenced on an Illumina platform and paired-end reads were generated. Library preparation and sequencing were carried out by Novogene Europe, Cambridge, UK. Gene set enrichment analysis was performed using GSEA Software v4.1.0 (Mootha et al., 2003; Subramanian et al., 2005) and the data deposited at the GEO repository under accession number GSE159606.

RNA-seq studies with LAPC-4 cells were carried out after treating the cells with vehicle (DMSO) or 5 μM A4B17 or enzalutamide. RNA preparation and sequencing was performed as described above by Novogene Europe. The raw gene expression was normalized with DESeq2 (Love et al., 2014) and the data deposited at the GEO repository under accession number GSE182278. Differential gene expression was determined for enzalutamide or A4B17 against vehicle samples (p(FDR)≤0.05). No threshold was applied for fold change.

Quantitative RT-PCR experiments

Select target genes were analyzed by RT-PCR experiments with RNA from the samples used for the RNA-seq analysis or from PC3, DU145, 22Rv.1 cells and from tumors collected at termination of the xenograft mouse experiments. RNA for qRT-PCR was isolated as described above and cDNA was synthesized with random primers using M-MLV Reverse Transcriptase (Promega, Walldorf, Germany). PCR analysis was carried out using the SYBR Green GoTaq PCR mix (Promega, Walldorf) with specific gene primers and Rib36B4 as a housekeeping gene.

Single-molecule tracking analysis

The SMT data were taken with a custom-built widefield microscope with single-molecule sensitivity described earlier (Li et al., 2016). The mEos2-AR fusion protein was photoconverted to its red fluorescent form by a weak 405 nm irradiation (0.9–1.7Wcm^{-2}) to ensure a small number of active molecules in each frame; 630Wcm^{-2} of 561 nm laser light was used for fluorescence excitation. For each cell, 4,000 frames with an exposure time of 30 ms each were acquired under live-cell conditions (37°C, 5% CO_2).

For image analysis, we used a-livePALM software (Li et al., 2013b), which localizes individual molecules in each frame. Closely adjacent locations in successive camera frames were linked to obtain single-molecule trajectories (Manley et al., 2008). Only those extending over at least five frames were used to calculate mean square displacements,

$$MSD(t) = \langle (x_{i+n} - x_i)^2 \rangle + \langle (y_{i+n} - y_i)^2 \rangle = 4Dt. \qquad \text{(Equation 1)}$$

Here, x_i and y_i are Cartesian coordinates of the molecule at the ith position along the trajectory, and the angular brackets denote averages taken overall pairs of locations with the same time lag, $t = n\Delta t$, with n being the difference in the position index (or camera frame number) and Δt denoting the camera dwell time (30 ms). From the MSDs, the diffusion coefficient D was computed by linear regression. Because the trajectories are typically short because of photobleaching of mEos2, there is a large uncertainty in the determination of D for an individual trajectory, in particular for small D. Therefore, on average 6,000 trajectories were recorded and analyzed for each experiment. The data on all cells were compiled in histograms. These were fitted with three Gaussians corresponding to one population of fast and two populations of slowly moving ARs, taking the widths and the center positions of the Gaussians representing the fractions as shared parameters in the simultaneous fit of all histograms. From the areas of the Gaussians, we calculated the relative fractions of the populations, peak positions yielding average D values, and standard deviations (widths, given as log (FWHM/$\mu m^2 s^{-1}$) reflecting mainly the large uncertainties in the MSD determination from short trajectories.

NMR

^{15}N-labelled BAG domain was generated by expressing the pET.His6.GB1a.Tev.BAGD in *E. coli* strain BL21 (DE3), grown in M9 minimal medium supplemented with 0.5 g/L $^{15}NH_4Cl$. The ^{15}N-BAG domain was cleaved off by Tev to remove the His.GB1 tag on Ni-agarose beads (Biozol, Eching, Germany). For interaction studies, peptides (synthesized at IGBMC, Strasbourg, France) were dissolved at 1.5 mM concentration in either phosphate buffer or DMSO and dialyzed overnight against phosphate-buffered saline (PBS) buffer, to which 2 mM DTT was added. The peptides were added to 50 μM ^{15}N-BAGD in PBS/DTT to a final concentration of 300 μM and transferred to a 5 mm NMR tube. ^{1}H^{15}N-HSQC spectra were measured on an Avance III 600 MHz spectrometer (Bruker BioSpin GmBH, Rheinstetten, Germany) equipped with a TXI-cryoprobe and Z-gradients. Spectra were acquired with 16 scans per increment, 2048 points in the direct and 256 points in the indirect dimension. The temperature was set to 26.7°C. Spectra were calibrated, processed and analyzed with Topspin (Bruker BioSpin GmbH, Rheinstetten, Germany). Chemical shifts changes (CSP) were calculated with the following equation: $CSP = \sqrt{(\partial CS(^1H)^2 + (0.1\ \partial CS(^{15}N)^2))}$ with CS being the chemical shift in Hz of ^{1}H and ^{15}N resonances, respectively.

Bulk synthesis of 2-(4-fluorophenyl)-5-(trifluoromethyl)-1,3-benzothiazole (A4B17)
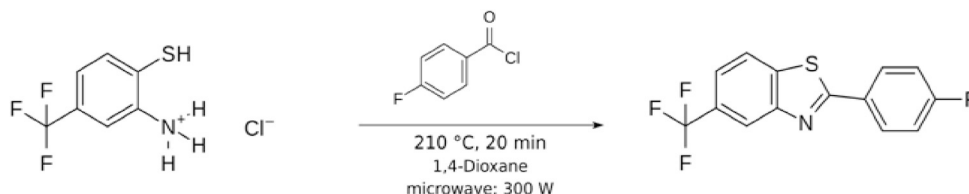
Formula: $C_{14}H_7F_4NS$; Molecular Mass: 297.2707; Exact Mass: 297.0235. Smiles: Fc1ccc(cc1)c1nc2c(s1) ccc(c2)C(F)(F)F; InChIKey: HVPGYAGVCOFPJH-UHFFFAOYSA-N

A mixture of 2-amino-4-(trifluoromethyl)benzenethiol; hydron; chloride (1.00 g, 4.35 mmol, 1.00 equiv) and 4-fluorobenzoyl chloride (759 mg, 566 μL, 4.79 mmol, 1.10 equiv) in dioxane (8 mL) was heated at 210°C under microwave irradiation for 20 min (max. power 300 W). The reaction mixture was diluted with methylene chloride (50 mL) and washed with aq. $NaHCO_3$ (50 mL). The organic solution was dried overNa_2SO_4 and filtered. As preparation for the column chromatography (dryload), Celite (3 g) was added to the filtrate and the resulting mixture was evaporated to dryness. The adsorbed crude product was purified via flash-chromatography (Interchim devices puriFLASH 5.125) on silica gel (PF-15SIHP-F0080) using cyclo-hexane/ethyl acetate 0%–10% ethyl acetate in 25 column volumes (1 column volume = 173.2 mL; flow: 34 mL/min). The isolated product 2-(3-fluorophenyl)-1,3-benzothiazole (1.22 g, 4.10 mmol) was obtained as colorless solid in 94% yield. R_f = 0.67 (cyclohexane/ethyl acetate 4:1).

^{1}H NMR (400 MHz, Chloro-form-d [7.27 ppm], ppm) δ = 8.33 (s, 1H), 8.13–8.08 (m, 2H), 8.01 (d, J = 8.6 Hz, 1H), 7.63 (dd, J = 1.1 Hz, J = 8.4 Hz, 1H), 7.24–7.19 (m, 2H); ^{13}C NMR (100 MHz, Chloro-form-d [77.0 ppm], ppm) δ = 168.7, 164.8 (d, J = 253.5 Hz), 153.7, 138.4, 129.7 (d, J = 8.5 Hz, 2C), 129.4 (d, J = 3.1 Hz), 129.1 (q, J = 32.4 Hz), 124.2 (q, J = 272.3 Hz), 122.2, 121.5 (q, J = 3.9 Hz), 120.3 (q, J = 3.9 Hz), 116.3 (d, J = 22.3 Hz, 2C); ^{19}F NMR (376 MHz, ppm) δ = −61.81, −107.74. MS (EI, 70 eV, 50°C), m/z (%): 297 (100) [M]+, 176 (12), 157 (16), 132 (10). HRMS–EI ($C_{14}H_7NF_4S$) (m/z): [M]$^+$ Calcd 297.0230; Found 297.0232. IR (ATR, v̄) = 3065 (vw), 2922 (vw), 1904 (vw), 1766 (vw), 1662 (vw), 1640 (vw), 1599 (w), 1589 (w), 1520 (w), 1485 (s), 1422 (w), 1408 (w), 1326 (vs), 1299 (w), 1258 (s), 1251 (s), 1235 (s), 1225 (s), 1214 (m), 1167 (s), 1149 (vs), 1112 (vs), 1102 (vs), 1077 (vs), 1055 (vs), 1011 (w), 989 (w), 966 (vs), 911 (m), 884 (s), 840 (vs), 815 (vs), 762 (m), 735 (w), 718 (w), 701 (vs), 669 (s), 640 (w), 623 (m), 609 (m), 589 (w), 551 (w), 534 (s), 506 (s), 459 (m), 445 (w), 425 (w), 380 (m) cm^{-1}.

Additional information on the chemical synthesis is available via Chemotion repository: https://doi.org/10.14272/reaction/SA-FUHFF-UHFFFADPSC-HVPGYAGVCO-UHFFFADPSC-NUHFF-NUHFF-NUHFF-ZZZ.1.

Additional information on the analysis of the target compound is available via Chemotion repository: https://doi.org/10.14272/HVPGYAGVCOFPJH-UHFFFAOYSA-N.3.

In vivo experiments

Zebrafish toxicity assay

Zebrafish embryos were transferred to 6-well plates 4 h after fertilization (hpf) in 12 mL of fish water containing vehicle (0.5% DMSO), A4B17 or enzalutamide (10 μM or 30 μM) (SelleckChem, Munich, Germany) dissolved in DMSO (final concentration 0.5%). Each well contained 24 embryos and the medium was replenished once a day and dead embryos were discarded. The toxicity assay was conducted in two parts: Part 1. Twelve embryos from the treatment group were placed each in a 384-well plate and imaged at 24 and 48 hpf and visually inspected for dead embryos. Part 2. The remaining 12 embryos were also transferred each to the 384-well plate and imaged at 72 and 96 hpf. The experiment was performed two times on two different days giving a total of 48 embryo replicates for the analysis. For imaging, an automated Scan^R IX 81 microscope (Olympus, Hamburg, Germany) was used.

The data was analyzed at four different developmental stages (24, 48, 72 and 96 hpf) for two endpoints: (1). Mortality, which was calculated as: (number of dead embryos/total number of exposed embryos) x 100; (2). Hatching and deformities: identified by visual inspection.

Mouse xenograft experiments

Determination of optimal concentrations. A4B17 (synthesized in house) and enzalutamide (abcr GmbH, Karlsruhe, Germany) were prepared in corn oil (Sigma, Steinheim, Germany) 1.0% dimethyl sulfoxide (DMSO) (Carl Roth, Karlsruhe, Germany). Male athymic nude-Foxn1^{nu} mice (Envigo) (6–7 weeks old) were randomized into five groups (3 mice per group) and treated daily for 14 days by oral gavage as follows: (1) Control group (Vehicle) (corn oil, 1.0% dimethyl sulfoxide (DMSO), (2) enzalutamide (Enza group, 10 mg per kg body weight), (3) A4B17 group, 30 mg per kg body weight) and, (4) A4B17 group (15 mg per kg body weight) and (5) A4B17 group (7.5 mg per kg body weight). Mice were sacrificed, prostate and seminal vesicles and other organs were removed and weighed.

Xenografts. LAPC-4 cells (2 million) were suspended in 100 μL PBS: Matrigel (Corning NY USA 1:1) and injected subcutaneously into both flanks of 6–7 weeksold male athymic nude-Foxn1^{nu} mice. The mice were castrated when the tumor volumes were around 50–100 mm^3. After 7 days, mice were randomized into four groups (7 mice per group) and treated daily by oral gavage as follows: (1) Control group (Vehicle) (corn oil, 1.0% dimethyl sulfoxide (DMSO), (2) enzalutamide (Enza group, 10 mg per kg body weight), (3) A4B17 group (30 mg per kg body weight) and, (4) A4B17 group (15 mg per kg body weight). Body weight and tumor volumes were measured twice a week. Tumor volume was measured with a digital vernier caliper and calculated using the formula length×heigth×width×0.5236 and recorded relative to the starting volume which was nominally set at 100%. After 34 days mice were sacrificed and the tumors removed and photographed. Tumor growth inhibition was calculated as TGI (%) = $(V_c - V_t)/(V_c - V_o) \times 100$, where V_c, V_t are the medians of the control and treated groups at the end of the treatment respectively, and Vo at the start. Percent body weight change was calculated using the following formula: group percent weight change = [(new weight - initial weight)/initial weight] x 100].

QUANTIFICATION AND STATISTICAL ANALYSIS

All experiments were performed with three or more replicates. Differences between two groups were analyzed by Student's *t* test and multiple comparison were determined by one-way ANOVA. If there were two factors (such as dose and time) investigated, data were analyzed by two-way ANOVA followed by a post hoc test. Data were expressed as means $\pm$ SEM, and $p < 0.05$ was considered significant. All analyses were performed using Microsoft Excel 2010 and GraphPad Prism 8 software.